CHALMERS
UNIVERSITY OF TECHNOLOGY

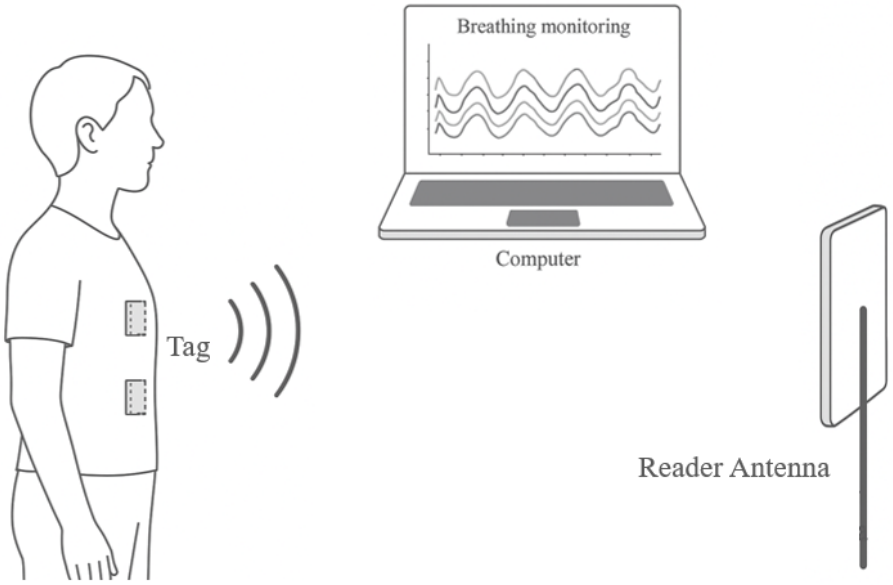

Breathing Monitoring with RFID Sensing

Tag Antenna Design and Signal Processing

Master's thesis in Electrical Engineering

ZICHEN MA and JIAQI WU

DEPARTMENT OF Electrical Engineering
CHALMERS UNIVERSITY OF TECHNOLOGY
Gothenburg, Sweden 2025
www.chalmers.se

Master's thesis 2025

Breathing Monitoring with RFID Sensing

Tag Antenna Design and Signal Processing

ZICHEN MA and JIAQI WU

CHALMERS
UNIVERSITY OF TECHNOLOGY

Department of Electrical Engineering
Division of Biomedical Engineering
Chalmers University of Technology
Gothenburg, Sweden 2025

Breathing Monitoring with RFID Sensing
Tag Antenna Design and Signal Processing
ZICHEN MA and JIAQI WU

Supervisor: XueZhi Zeng, Electrical Engineering
Examiner: XueZhi Zeng, Electrical Engineering

Master's Thesis 2025
Department of Electrical Engineering
Biomedical Engineering
Chalmers University of Technology
SE-412 96 Gothenburg
Telephone +46 31 772 1000

Typeset in LaTeX
Printed by Chalmers Reproservice
Gothenburg, Sweden 2025

Breathing Monitoring with RFID Sensing
Tag Antenna Design and Signal Processing
JIAQI WU and ZICHEN MA
Department of Electrical Engineering
Chalmers University of Technology

Abstract

Real-time monitoring of respiratory function plays an essential role in both clinical diagnosis and pulmonary rehabilitation. In this work, we proposed a novel respiratory monitoring solution based on ultra-high frequency (UHF) radio-frequency identification (RFID) technology for local measurement of breathing at multiple locations simultaneously. A respiratory monitoring system was built using commercial RFID devices, and a signal processing algorithm was developed to extract respiratory features. The results demonstrate high accuracy in both respiratory rate and temporal pattern compared with a reference piezoelectric (PZT) respiratory belt. Moreover, two compact tag antennas were designed and optimized to operate on the human body. Two different methods, stencil printing and copper tape engraving, were used for tag antenna fabrication, with advantages and challenges analyzed. Overall, our study suggests that RFID technology holds a big potential for non-invasive and localized respiratory monitoring.

Radio frequency identification(RFID); Respiratory monitoring; Flexible antenna; Wearable sensor; Bioelectromagnetic simulation; Non-invasive detection.

Acknowledgements

We would like to express our gratitude to all those who supported us during this thesis.
First and foremost, we would like to thank our supervisor and examiner, Xuezhi Zeng, for her valuable guidance and continuous support throughout the research process. We are also grateful to our families and friends for their encouragement and understanding, which helped us stay motivated while completing our thesis. Finally, we gratefully acknowledge the support and resources provided by the faculty of the School of Materials Science and the related laboratories during the experimental and research phases of this thesis. Their contributions were essential to the successful completion of our work.

Zichen Ma and Jiaqi Wu, Gothenburg, June 2025

List of Acronyms

Below is the list of acronyms that have been used throughout this thesis listed in alphabetical order:

UHF	Ultra High Frequency
RFID	Radio Frequency Identification
PFT	pulmonary function test
FVC	Forced Vital Capacity
FEV_1	Forced Expiratory Volume in 1 second
TLC	Total Lung Capacity
DLCO	Diffusing Capacity for Carbon Monoxide
CT	computed tomography
RUT	Right Upper Thorax
LUT	Left Upper Thorax
RLT	Right Lower Thorax
LLT	Left Lower Thorax
RA	Right Abdomen
LA	Left Abdomen
VNA	vector network analyzer
PZT	Piezo-Electric Respiration Sensor

Contents

List of Figures

List of Tables

1

Introduction

Respiratory diseases represent a major global health burden, with increasing prevalence and mortality rates in recent years. The COVID-19 pandemic alone claimed the lives of over 5.7 million people within just 24 months, primarily due to respiratory complications[1]. However, even before the pandemic, respiratory illnesses were consistently among the top ten causes of death globally[2]. Common chronic respiratory diseases include chronic obstructive pulmonary disease (COPD), asthma, occupational lung diseases, and pulmonary hypertension. Among them, COPD has emerged as a particularly significant cause of morbidity and mortality. Between 2009 and 2019, the global mortality rate of COPD increased by 35.4%, and projections by the World Health Organization estimate that COPD will become the third leading cause of death worldwide by 2030[3]. Therefore, the ability to accurately monitor respiratory patterns and detect early signs of respiratory distress is crucial for timely intervention and improved patient outcomes[4].

Changes in respiratory function serve as important indicators of various disease states and physiological conditions[5]. The normal respiratory rate ranges from 12 to 20 breaths per minute. In pathological conditions, the respiratory rate often increases as a compensatory mechanism to maintain adequate oxygen intake or carbon dioxide elimination[6]. In cases of neuromuscular disease, hypoventilation or abnormal breathing patterns may occur, leading to elevated rates during exertion and insufficient ventilation at rest[7]. As such, respiratory monitoring systems that capture these changes are widely employed in clinical diagnosis, rehabilitation, and health monitoring[8].

Currently, common clinical methods for respiratory function monitoring include pulmonary function testing, inductive plethysmography, ultrasound examination, and imaging technologies such as computed tomography (CT) and infrared cameras[9, 10, 11]. Pulmonary function testing including spirometry is widely used in clinical practice to measure lung capacity and airflow, providing important evidence for assessing lung function. However, it typically requires active patient cooperation and is only suitable for static detection scenarios[5]. Inductive plethysmography detects respiratory movements by placing belts around the chest and abdomen, but may cause discomfort and have practical limitations in long-term monitoring applications [12]. Ultrasound examinations and CT scans can provide high-resolution information on lung mechanics, but they typically require specialized equipment and personnel, and are not suitable for continuous or mobile monitoring[13, 11]. Infrared cameras are non-contact and can effectively visualize breathing patterns, but they are sensitive to environmental conditions and system setup complexity[14].

In recent years, with the rapid development of wireless sensing and wearable technologies, portable, low-cost, and non-invasive monitoring devices have attracted increasing attention. Among these, UHF RFID technology has gradually become one of the important research directions in the field of health monitoring in both clinical and home settings due to its advantages of passive operation, small size, low cost, and robust wireless communication capabilities[15, 16]. Additionally, RFID systems require relatively low patient cooperation and provide real-time respiratory data, making them particularly suitable for long-term respiratory assessment and overcoming many limitations of other respiratory measurement methods. Existing robust RFID-based respiratory monitoring systems can accurately estimate respiratory rate and detect apnea under environmental interference, with an average error of only 0.5 breaths per minute[17]. Moreover, RFID-based respiratory monitoring methods have been demonstrated to be feasible, enabling accurate multi-person tracking as well as multi-localized measurements on the chest and abdomen simultaneously[18]. However, commercial RFID tags are generally designed for air environments, the resonant frequency of the antenna will shift significantly after being attached to the human body surface, thus affecting the stability and effectiveness of signal reading[19]. Therefore, developing a flexible RFID antenna optimized for body-worn applications and improving its impedance matching in the human environment has become a key technical challenge for achieving reliable respiratory monitoring. Moreover, to meet practical needs in clinical and home rehabilitation environments, further improvements in user comfort and antenna encapsulation are required. Another important aspect is the processing of RFID based measurement data to extract features or parameters of clinical interest.

This work focuses on these two main aspects, with the following specific objectives:

- To build an experimental platform based on a respiratory simulator to enable real-time signal acquisition and analysis;
- To develop data processing algorithms capable of accurately extracting respiratory frequency and amplitude characteristics, and to evaluate the overall system performance.
- To design and optimize a flexible UHF RFID tag antenna suitable for body-worn use and mitigate frequency detuning caused by human loading effects;
- To develop an antenna encapsulation scheme and fabricate practical tag prototypes;

The remainder of this paper is organized as follows: Chapter 2 introduces some basic principles of RFID-based respiratory monitoring. Chapter 3 includes the experimental setup, data processing methods and evaluation of the overall monitoring system performance. Chapter 4 describes the design, simulation, fabrication, and evaluation of the antenna. Chapter 5 provides an analysis of the results and causes of the experiment and explores possible future improvements. Finally, Chapter 6 summarizes the research findings and discusses future research directions.

2

Theory

2.1 Radio Frequency Identification (RFID) Basics

RFID is a non-contact automatic identification technology that uses electromagnetic fields to identify and track objects. It is widely used in logistics, access control, retail, and increasingly in biomedical applications due to its wireless, passive, and low-power properties.

2.1.1 RFID System Basics

An RFID system enables the wireless or contactless transmission of digital IDs and other data between RFID tags and readers through electromagnetic waves. By tagging physical objects, organizations, enterprises, and consumers can identify, verify, track, monitor, and interact with each item via a unique digital ID. In simple terms, an RFID system consists of three components: RFID tag, RFID readers (also known as interrogators), and software (middleware) that transmits the acquired data to IT systems or the Internet of Things (IoT) platforms[15]. As shown in Figure

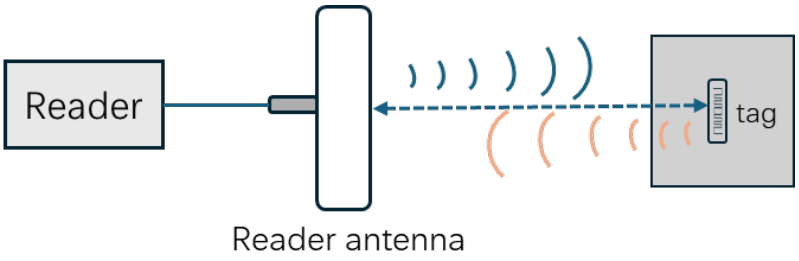

Figure 2.1: RFID measurement system.

2.1, When the reader intends to communicate with an RFID tag, it modulates and sends out the signal through reader antenna and the tag is activated by the signal. Once activated, the tag sends out a backscatter signal to the reader antenna. The received backscattered signal can be represented as[20]:

$$S(t) = A(t)e^{-j\phi(t)}, \tag{1}$$

where $A(t)$ is the amplitude of the signal and $\phi(t)$ is the phase value of the signal. Both the Received Signal Strength (RSS) and the phase of the signal received by

the reader antenna are affected by the distance between the tag and the antenna, denoted as d. The relationship between the phase ϕ and the distance d can be modeled as[20]:

$$\phi = \left(2\pi\frac{2d}{\lambda} + \theta\right) \mod 2\pi, \tag{2}$$

where λ is the wavelength of the signal and θ is a diversity term caused by hardware imperfection of the reader and tag.

RFID Tag

RFID tags come in various shapes and sizes and can be either passive or active. The most common type is the passive tag, which does not require an internal power source such as a battery. A passive tag typically consists of an RFID inlay and an outer casing for physical protection. The inlay comprises a small silicon microchip that stores the digital ID and other data, attached to an antenna printed on a thin substrate such as paper or plastic (PET) film. The antenna receives radio frequency signals from the reader and transmits them to the chip, which then uses the harvested energy to send a return signal to the reader[21].

Types of RFID Systems

RFID systems operate across three main radio frequency bands: low frequency (LF), high frequency (HF), and ultra-high frequency (UHF). These systems differ in terms of application, maximum reading range, and the types of tags and readers used[22]. Most LF systems operate in the 125-134 kHz band and offer reading distances of up to 10 cm. They are commonly used for animal identification, access control, vehicle entry, and environments with dense liquids or metal. HF and NFC RFID systems operate at 13.56 MHz, with reading distances ranging from near contact to approximately 50 cm. Typical applications include library media management, industrial automation, ID cards, contactless payment (via NFC-enabled cards or smartphones), and consumer engagement. HF tags require dedicated readers, while NFC tags can be read by most smartphones within a few centimeters[23]. UHF RFID systems operate in the 860-960 MHz frequency range. Their typical reading distance ranges from close proximity to over 20 meters, making them suitable for a wide range of applications including inventory and supply chain management, medical monitoring, smart manufacturing, airline baggage tracking, and sports timing [21].

Within the UHF frequency range, there are two major regional sub-bands defined by regulatory authorities: the European Telecommunications Standards Institute (ETSI) defines the 865-868 MHz band, while the U.S. Federal Communications Commission (FCC) specifies the 902-928 MHz band[24]. Compared to LF and HF systems, UHF systems support longer reading distances, allow for cost-effective and flexible tag design in various shapes and sizes, and enable high-speed bulk tag reading. However, they are more susceptible to RF interference from metal, conductive materials, or liquids.

For our thesis, passive tags are ideal due to their compact size, structural simplicity, long operational lifespan, and low cost. Meanwhile, the UHF frequency band

provides extended reading range and high data transmission speed, making it the most suitable choice for our medical respiratory monitoring application.

2.1.2 RFID-Based Respiratory Monitoring

The principle of using RFID for respiratory monitoring relies on the high sensitivity of radio frequency signals to subtle movements and environmental changes. During respiration, the expansion and contraction of the chest and abdomen cause slight displacements of the RFID tag, which in turn change the distance between the tag and the reader antenna. This distance variation leads to measurable phase shifts in the backscattered signal, thereby enabling respiration-induced motion to be captured in real time by the RFID reader[25]. By applying signal processing techniques to the received data, the system can reconstruct the respiratory waveform and determine the breathing rate.
Key signal features that can be extracted from the backscattered RFID signal for motion analysis include the Received Signal Strength Indicator (RSSI), phase, and Doppler frequency shift. These physical quantities are sensitive to small displacements and can be continuously monitored to detect respiratory patterns. In our configuration, we rely on phase variations to quantify the displacement of the chest wall caused by breathing. Due to the high temporal resolution of phase data provided by RFID systems, meaningful respiratory information such as frequency, amplitude, and pattern changes can be extracted from these weak fluctuations using signal processing techniques like phase unwrapping and filtering. Compared to electrode- or pressure-based sensors, the RFID monitoring approach offers advantages such as non-contact operation, passive deployment without batteries, and low cost. These features make it especially suitable for portable health monitoring devices and remote telemedicine applications.

The Effect of Biological Tissue

When the RFID tag works in free space, the radiation characteristics and resonant frequency of its antenna are designed according to the dielectric characteristics of air. However, the respiratory monitoring involves placing tags on human chest and abdomen, when the tag is attached to the human surface, the dielectric constant and conductivity of the surrounding environment change significantly, especially the biological tissues such as skin, fat and muscle will cause the absorption and reflection of electromagnetic waves [26]. Figure 2.2 shows the hierarchical model of human chest. This human body loading effect will lead to the decrease of antenna resonance frequency, impedance mismatch and gain, thus affecting the identification distance and signal stability of the tag. In order to ensure that the tag still has good performance in the actual wearing environment, the electromagnetic characteristics of the tissue layer must be considered in the antenna design stage and optimized by simulation[27].

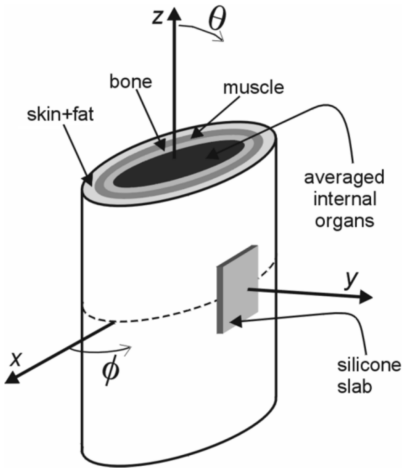

Figure 2.2: Hierarchical model of human chest[26].

2.1.3 Antenna Theory

The classical radar equation is fundamental for understanding the power relationship between a transmitter, a target, and a receiver in wireless sensing systems such as RFID. It quantitatively relates the transmitted power, antenna gains, target characteristics, and the distance between the transmitter and the target to the received power. The radar equation for a monostatic radar system (where the transmitter and receiver share the same antenna) is expressed as:

$$P_r = \frac{P_t G_t G_r \lambda^2 \sigma}{(4\pi)^3 d^4} \tag{2.1}$$

where:

- P_r is the received power at the radar receiver (W),
- P_t is the transmitted power from the radar antenna (W),
- G_t is the gain of the transmitting antenna (unitless),
- G_r is the gain of the receiving antenna (unitless),
- λ is the wavelength of the transmitted signal (m),
- σ is the radar cross section (RCS) of the target, representing the effective reflective area (m^2),
- d is the distance between the radar antenna and the target (m).

This equation assumes free-space propagation without considering multipath effects or other environmental losses. The received power P_r decreases with the fourth power of the distance d, reflecting the two-way (transmit and receive) path loss in radar and RFID systems. Understanding this relationship is essential for analyzing antenna performance parameters such as gain, impedance matching, and reflection coefficients, which directly influence system read range and sensitivity.

Antenna Gain

Antenna gain describes the ability of an antenna to direct radiated power in a specific direction compared to an isotropic radiator. It is expressed in dBi (decibels relative to an isotropic antenna). In RFID systems, higher antenna gain contributes

to improved signal strength and longer read range [28].
In passive UHF RFID systems, where tags rely on backscattered signals and power harvested from the reader, antenna gain significantly affects both forward-link power delivery and backscatter signal strength. A well-optimized gain pattern ensures that the antenna effectively radiates towards the reader.

Reflection Coefficient

The reflection coefficient, commonly denoted as S_{11}, measures how much power is reflected back at the antenna port due to impedance mismatch. It is typically presented in decibels, and an S_{11} value below –10 dB is generally considered acceptable for good matching [15].
A high reflection coefficient implies significant power is reflected instead of being radiated, reducing the effective radiated power and thus limiting communication range. In body-worn RFID systems, tissue-induced detuning can cause poor S_{11} characteristics unless the antenna is designed and matched under loaded conditions.

Chip Impedance Matching

Maximum power transfer occurs when the complex conjugate of the antenna impedance Z_{ant} matches the chip impedance Z_{chip}, i.e., $Z_{\text{ant}} = Z^*_{\text{chip}}$. In passive RFID tags, impedance matching is crucial because the chip has limited input power tolerance [29].
Mismatch between chip and antenna impedance leads to reflection and inefficient energy harvesting, directly affecting the tag's ability to power up and respond. Therefore, antenna tuning must consider both the chip's reactive behavior and the detuning effects of proximity to human tissue [26].

Radiation Pattern

A three-dimensional radiation pattern provides a visual map of an antenna's normalized field strength over all spatial directions by projecting the gain (or field intensity) onto a spherical surface. In this representation, the main lobe appears as the largest bulge—indicating the direction of strongest radiation—while side and back lobes show where energy "leaks" outside the intended beam. The shape and sharpness of the main lobe directly reflect the antenna's directivity and ability to focus energy, and the relative size of secondary lobes indicates how well the antenna suppresses unwanted radiation. Such 3D visualization is invaluable for assessing overall antenna performance, particularly in determining how effectively the antenna can direct power toward a reader or sensor and reject interference from other directions [28]. Figure 2.3 shows an example of 3D radiation pattern.

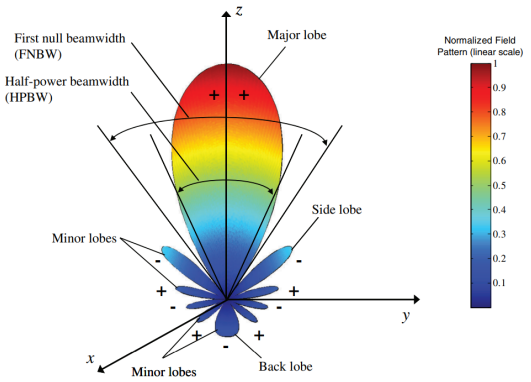

Figure 2.3: A symmetrical three-dimensional polar pattern with a number of radiation lobes[28]

In addition to the full 3D radiation pattern, antenna performance is often characterized by two-dimensional cuts in the principal planes: the E-plane ($\phi = 0°$) and H-plane ($\phi = 90°$). In the E-plane cut, which lies in the plane containing the electric field vector and the antenna's main axis, the gain is plotted as a function of the elevation angle θ to reveal the shape, peak magnitude, and beamwidth of the main lobe and any side lobes. Conversely, the H-plane cut, taken in the plane containing the magnetic field vector, shows how the antenna radiates in the orthogonal direction and often exhibits a different beam spread and sidelobe structure. By examining both cuts, each showing the peak gain position, 3 dB angular width, and relative sidelobe levels—one can fully assess the antenna's directional behavior and polarization characteristics in key orientations.

Read Range

Several factors affect RFID read range: antenna gain, transmitted power, chip sensitivity, impedance match, polarization, and environmental losses. For wearable applications, tissue absorption and tag orientation also have a significant impact [30].
The theoretical read range R can be estimated using the Friis transmission formula:

$$R = \frac{\lambda}{4\pi}\sqrt{\frac{P_t G_t G_r \tau}{P_{\text{th}}}} \tag{2.2}$$

where λ is the wavelength, P_t is the reader power, G_t and G_r are the transmit and receive antenna gains, τ is the power transmission coefficient (function of impedance match), and P_{th} is the chip activation threshold.

3

RFID-based Breathing Monitoring System

This chapter presents the complete development and performance evaluation of a real-time respiration monitoring system based on passive UHF RFID technology. The first section describes the system's development, including hardware setup, real-time data acquisition and visualization platform, and signal processing algorithms used to extract respiratory information from raw phase data. The second section provides a comprehensive evaluation of the system under various conditions, focusing on motion robustness, the impact of tag mounting media, and validation against a synchronized piezoelectric (PZT) belt reference.

3.1 Measurement System and Experimental setup

This section presents a real-time respiration monitoring system based on passive UHF RFID technology. The system integrates hardware employment, software development, and signal processing techniques to enable real-time tracking of respiratory motion. We first describe the experimental setup, including the antenna configuration strategy, followed by the implementation of a real-time data acquisition and visualization platform. Finally, the signal processing algorithms used to extract and validate respiratory features from raw RFID phase data are detailed.

3.1.1 Measurement System

This subsection details the Hardware configuration and software framework used to enable real-time RFID-based respiratory monitoring. It introduces the development of a custom software platform for data acquisition and visualization, which supports both real-time waveform display and offline analysis.

Hardware Configuration

- Reader: Impinj Speedway R420 UHF RFID reader
- Reader Antenna: Alien ALR-8698 Circular Polarized Panel Antenna
- Reader Configuration via Octane SDK: Session 0 and Dual Target reader mode were used to ensure continuous tag responses and a high-density data stream.
- Tag: AD Belt M730, 860-960 MHz, 73*17 mm

Data Acquisition and Real-time visualization To realize an RFID based real-time respiration monitoring system, we developed an integrated data acquisition, processing, and visualization software platform in Visual Studio Code using C# and the .NET framework.
Raw data packets—each containing the EPC, antenna port number, RSSI, raw phase (in radians), and a precise timestamp—were captured at approximately 10 Hz and buffered in memory. Simultaneously, the data were saved to CSV files for offline analysis and validation. After each buffer update, a processing routine was triggered to compute physical displacement from the unwrapped phase.
The platform incorporates real-time visualization using the ScottPlot library. The user interface consists of two main views:

- **All-Tags View:** Overlaid live waveforms of all tags is shown in figure 3.1
- **Individual-Tag View:** Separate live waveform display for each tag to facilitate detailed local analysis, is shown in figure 3.2

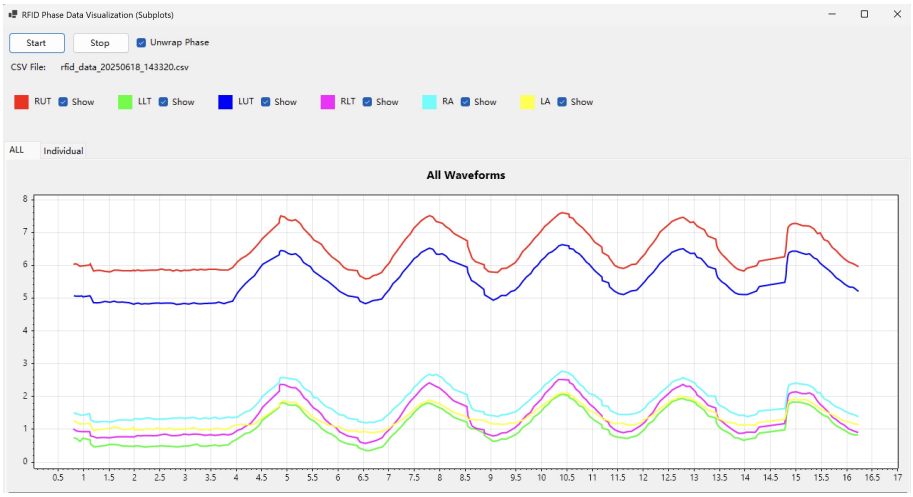

Figure 3.1: Overlaid Real-time waveform

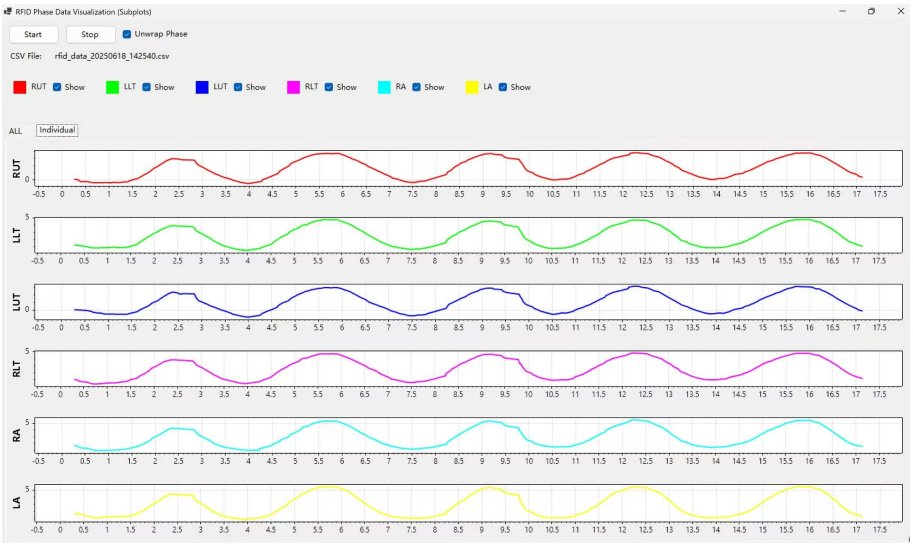

Figure 3.2: Real-time waveform for individual tag

3.1.2 Experimental Setup

This subsection describes the experimental procedures designed to evaluate the performance of the RFID-based respiratory monitoring system under different conditions. A series of experiments were conducted on both non-biological object and human subjects to validate the system's baseline accuracy in tracking displacement and examine the effects of different tag mounting materials. Finally, validation studies were carried out using piezoelectric (PZT) belt sensors as a reference under both 2-tag and 4-tag configurations, enabling a systematic comparison of RFID-derived respiratory signals with established ground truth measurements.

3.1.2.1 On non-biological medium

To isolate and verify the tag's inherent measurement accuracy, we attached a single tag to a cardboard box and moved the box forward and backward in small increments to check if the shifted distance on the signal is consistent with the actual distance. The setting is shown in Figure 3.3

(a) Tag and cardboard configuration

(b) Tag

Figure 3.3: Tag test on cardboard box

3.1.2.2 Human body test

To evaluate the effect of human skin on tag signal integrity, we conducted a series of controlled experiments. The RFID reader antenna was placed at a fixed position in front of the human subject. The subject was instructed to stand in a neutral upright posture, facing directly toward the reader. The antenna was positioned at a horizontal distance of approximately 1.5 meters from the chest wall, with a height of 1.3 meters from the floor, approximately aligned with the mid-thoracic level of an average adult. The subject remained stationary during data collection to avoid additional motion artifacts. All measurements were taken in a controlled indoor environment as shown in Figure 3.4.
Three experimental conditions were considered to investigate how varying degrees of body–antenna coupling affect respiratory signal quality:

- **Direct skin contact:** A commercial RFID tag was placed directly on the skin surface to investigate the influence of close electromagnetic coupling between the tag antenna and the human body.
- **Clothing-mounted:** The RFID tag was attached to a single layer of everyday clothing covering the chest or abdomen, simulating a practical deployment scenario where direct skin contact is avoided.
- **Clothing with belt insulation:** The RFID tag was fixed onto an elastic belt, and the belt was then worn over the same layer of clothing. This setup introduced an additional spacing layer between the tag and the skin, allowing assessment of performance under partial isolation from direct body contact.

Figure 3.4: Measurement setup

Furthermore, to validate our respiratory monitoring system, a piezoelectric (PZT) sensor with the 8-Channel biosignalsplux Kit are employed as a reference signal source to enable synchronized measurement and accuracy evaluation of the system's respiratory signals. As the subject inhales and exhales, the expansion and contraction of the thoracic or abdominal wall induce mechanical stress on the piezoelectric sensor, generating corresponding voltage signals[34].
To evaluate the spatial sensitivity and accuracy of RFID-based respiratory monitoring, we designed two deployment strategies: 2-tag and 4-tag configurations, with the PZT belt alternately positioned on the chest or abdomen.
In the 2-tag setup, two variations were tested: Upper chest and abdomen — One tag was placed on the upper chest and the other at the center of the abdomen, while the PZT belt was alternately positioned on the chest or abdomen in two separate trials (Figure 3.5a). This allowed direct comparison between RFID and belt measurements as well as assessment of regional differences in respiratory signal quality. Bilateral placement — Two tags were placed symmetrically on either side (left and right) of the upper chest or abdomen, with the belt positioned on the corresponding region (Figure 3.5b). This configuration was used to evaluate the consistency and symmetry of respiratory signals across lateral body positions and to examine whether bilateral sensing enhances robustness.
In the 4-tag setup, four tags were deployed simultaneously: two on the chest (RUT and LUT) and two on the abdomen (RA and LA). The belt was alternately placed on

the chest or abdomen in two separate trials (Figure 3.5c). This comprehensive configuration enabled investigation of multi-tag performance and potential interactions in a more complex sensing environment.

(a) 2-tag: upper chest and abdomen

(b) 2-tag: bilateral chest or abdomen

(c) 4-tag: RUT and LUT, RA and LA

Figure 3.5: Tag deployment strategy

3.1.3 Signal Processing Algorithm

Data processing was conducted using MATLAB, figure 3.6 illustrates the complete signal processing workflow used to extract and validate respiratory signal information from RFID phase data.

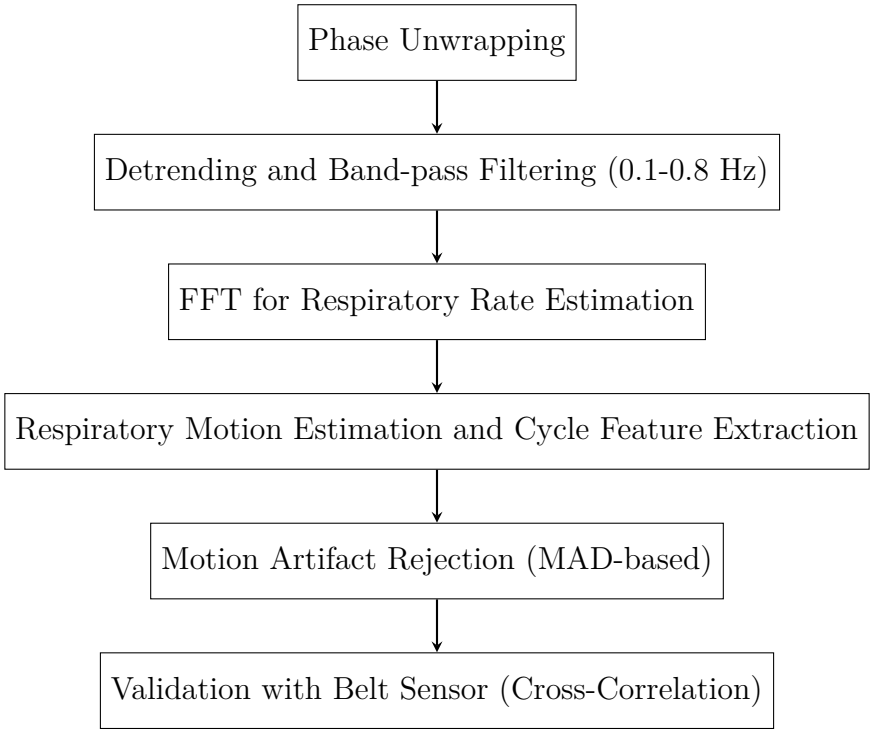

Figure 3.6: Signal processing pipeline for RFID-based respiratory monitoring.

The detailed implementation of each step is described as follows:

- Phase Ambiguity Correction and Unwrapping:
  Due to the $[0, 2\pi]$ constraint on RFID phase readings, abrupt $\pm\pi$ jumps occur. We first performed ambiguity correction by examining the phase difference between consecutive samples: if the difference approached $\pm\pi$, we added or subtracted π to the current sample to remove the jump. Next, phase unwrapping was applied: whenever the corrected phase difference between adjacent points approached $\pm 2\pi$, we cumulatively added or subtracted 2π to maintain a continuous phase trajectory. This yielded a smooth, unwrapped phase signal that more accurately reflects the subtle body movements result from breathing is shown in figure 3.7.

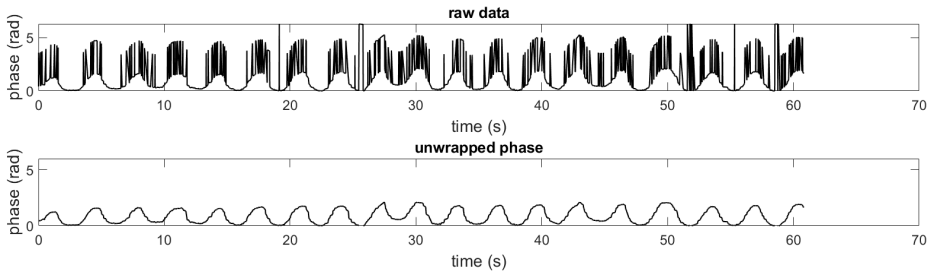

Figure 3.7: Raw data and unwrapped phase

- Extraction of unwrapped phase data and detrending:
  Figure 3.8 compares the original unwrapped phase (black line) with the detrended phase signal (blue line). Phase unwrapping effectively resolves abrupt phase jumps due to modulo 2π ambiguities inherent to RFID systems, yielding a continuous signal representation. Subsequently, detrending removes the slow baseline drift, which is likely caused by slight movements or environmental factors, emphasizing the respiratory-related variations and enabling more accurate analysis.

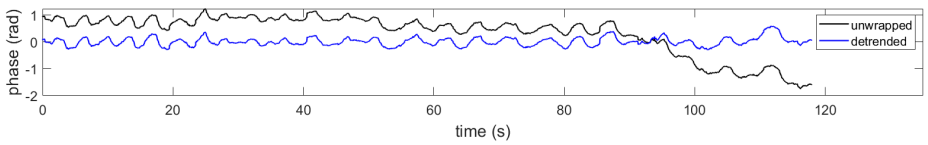

Figure 3.8: Unwrapped and detrended phase signals illustrating the removal of baseline drift.

- Application of a band-pass filter (0.1 Hz–0.8 Hz):
  Following baseline correction, filtering is applied to further improve signal quality. Figure 3.9 shows the detrended signal (black line) along with the filtered signal (blue line). The filtering process suppresses high-frequency noise and artifacts, clearly revealing a smoother respiratory waveform. This clean signal significantly improves the reliability and accuracy of subsequent respiratory rate extraction and respiratory pattern analysis.

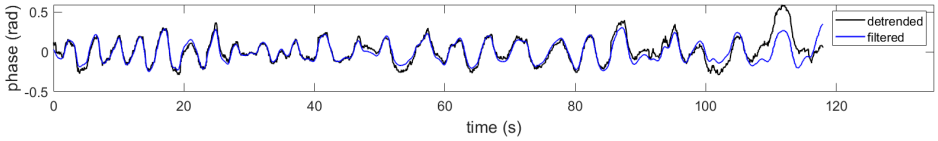

Figure 3.9: Detrended and filtered phase signals, demonstrating noise reduction and signal smoothing.

- Use FFT to calculate the respiratory rate:
  Figure 3.10 shows how FFT can accurately extract respiratory rate from periodic phase signals. The left plot shows a simulated respiratory signal in the time domain, representing chest wall motion at a breathing rate of 14 breaths per minute. The right plot displays the corresponding frequency spectrum obtained via FFT. A clear peak appears at approximately 0.233 Hz, which directly corresponds to the breathing frequency.

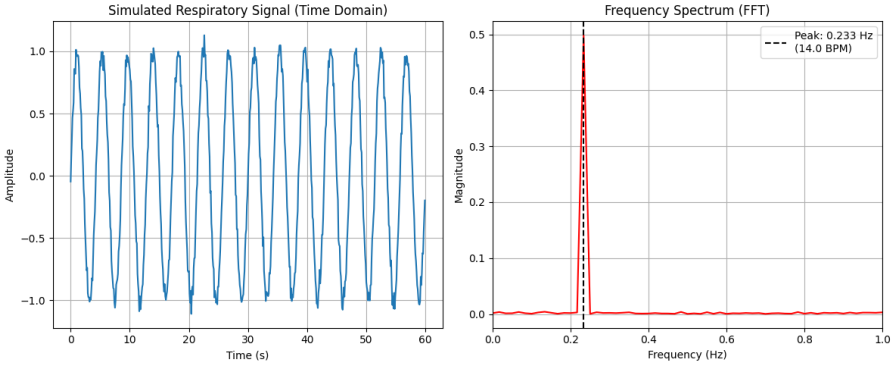

Figure 3.10: An example of respiratory signal time-frequency conversion

- Respiratory motion estimation and cycle feature extraction:
  The actual respiratory movement is calculated using the following equation:

$$\text{Movement (mm)} = \frac{1000 \cdot \phi \cdot \lambda}{4\pi} \tag{3.1}$$

  where ϕ represents the smoothed phase value, and λ is the wavelength of the signal (in meters). Peaks and troughs of the respiratory signal are detected by identifying local maxima and minima and a minimum peak-to-peak interval is enforced to ensure physiologically reasonable cycle detection, as illustrated in Figure 3.11. The amplitude of each respiratory cycle is computed using the difference between the peak and the average of the two adjacent troughs shown as Figure 3.12.

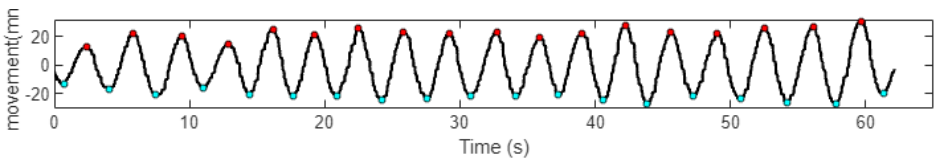

Figure 3.11: Detection of peaks and troughs

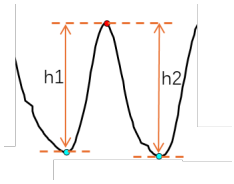

Figure 3.12: Amplitude of one respiratory cycle

- Implementation of a motion artifact rejection algorithm:
  The smoothed phase signal was segmented into overlapping windows based on a sliding-window median absolute deviation (MAD) test, and each segment's normalized MAD was computed. An adaptive threshold was set using the global MAD value, and any segment exceeding this threshold was identified as an artifact as shown in figure 3.13.

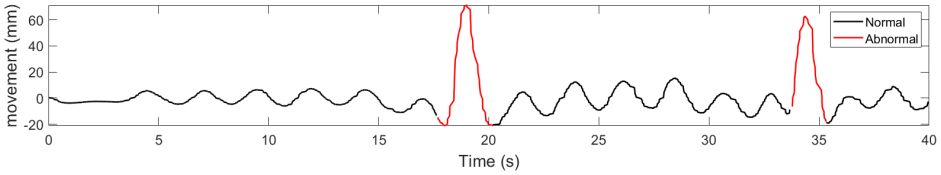

Figure 3.13: Abnormal detection

- Validation with piezoelectric (PZT) belt:
  To evaluate the accuracy of RFID-based respiratory detection, the tag signal is compared with the respiratory signal acquired from a PZT belt sensor. After normalization and resampling to ensure both signals are on the same temporal and amplitude scale, maximum cross-correlation is applied to determine the optimal time lag between the RFID and belt signals by shifting one signal across a range of time offsets and identifying the lag that yields the highest correlation coefficient as shown in Figure 3.14. This step compensates for latency introduced by differences in the devices' start-up times and processing pipelines. Then the cross-correlation coefficient is computed between the RFID tag and belt signals to evaluate their waveform similarity. A higher correlation indicates stronger linear similarity in the temporal dynamics of the two signals, suggesting better respiratory pattern agreement.

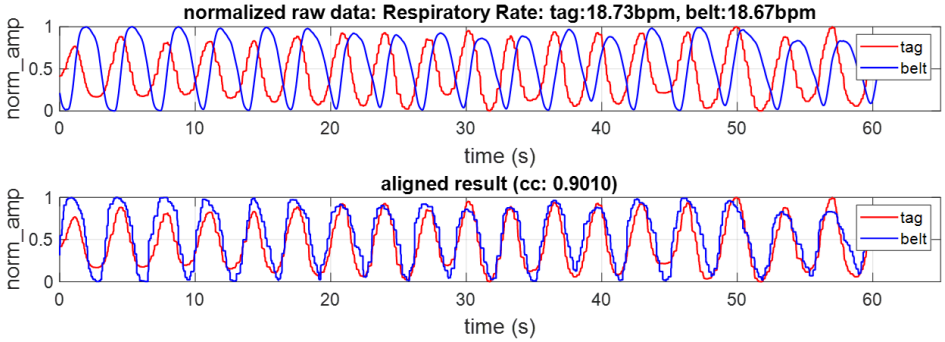

Figure 3.14: Alignment of tag and belt signals

3.2 Evaluation of System Performance

This section evaluates the performance of the RFID-based respiration monitoring system under various real-world conditions. The analysis focuses on the system's robustness against motion artifacts, different tag mounting conditions, and its accuracy in capturing respiratory dynamics using different tag deployment strategies. A synchronized piezoelectric (PZT) belt is employed as a reference to validate temporal alignment and assess the spatial consistency of respiratory signals acquired through the RFID system.

3.2.1 Random Motion Detection

To evaluate the robustness of the signal processing for motion artifacts detection, controlled body movements were deliberately introduced during normal breathing trials. These included speaking (20–25s), coughing (32–37s), and lateral shoulder movements (right shoulder: 44–49s; left shoulder: 53–58s).

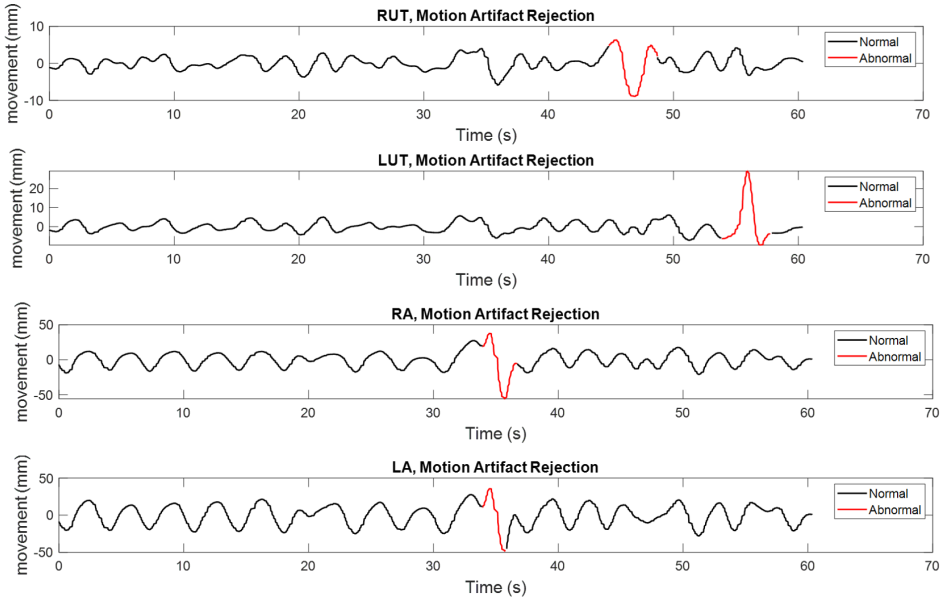

Figure 3.15: Random motion detection.

Figure 3.15 illustrates the performance of the abnormal cycle rejection algorithm. Signal segments identified as artifact-dominant are highlighted in red. The results show that speaking was not flagged as an anomaly, which is expected, as it typically involves minimal torso motion and does not significantly disrupt respiratory rhythm. In contrast, coughing was detected as an anomaly by both abdominal tags, likely due to the strong, abrupt contractions associated with intense coughing. However, it is worth noting that mild coughing may not introduce sufficient perturbation to be classified as random motion, and thus should not always be rejected.
Shoulder movements triggered spatially localized anomaly detection: right shoulder movement was detected by the right upper thoracic (RUT) tag, while left shoulder movement was captured by the left upper thoracic (LUT) tag. These motions were

not identified as anomalies by abdominal tags, highlighting the system's spatial selectivity and regional sensitivity to motion sources.

3.2.2 Effect of Object Material

When the tag was mounted on cardboard box, the system was able to accurately track displacement patterns corresponding to 1.5 cm, 2.5 cm, 4 cm, 6 cm and 0.8 cm of controlled motion as shown in Figure 3.16. These results validate that the tag and test process can capture subtle linear motion with high fidelity in free-space.

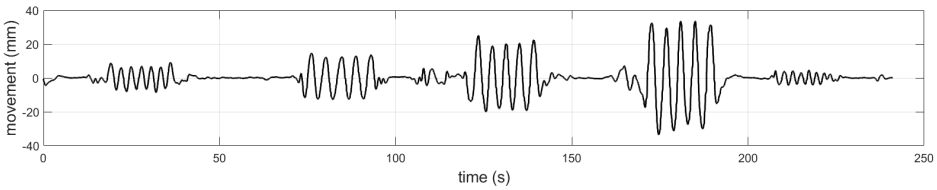

Figure 3.16: One tag on box and move the box

When the tag was placed in direct contact with the skin, however, the reader failed to receive any backscattered signal, which confirms that the lossy and high-permittivity characteristics of skin introduce significant detuning and absorption, severely impairing antenna performance and signal reception.

In contrast, when the tag was mounted on clothing covering the chest or abdomen, the resulting respiratory waveforms, as shown in Figure 3.17, clearly reflect cyclic breathing motion. On the abdomen, when the tag was placed directly on the clothing without additional insulation, the detected respiratory displacement on the abdomen reached an unusually large average amplitude of 47.8 mm—far exceeding the typical abdominal breathing range of 10–15 mm, but decreased to 7 mm when the tag was mounted on an elastic belt over the same clothing at the same anatomical location as shown in Figure 3.17b. This anomaly is likely due to strong electromagnetic coupling between the antenna and the underlying skin, potentially causing detuning effects that amplify phase fluctuations in a non-linear manner. The added separation between the antenna and the skin likely improved electromagnetic stability, while simultaneously reducing mechanical coupling to the body as the abdomen tends to have thicker subcutaneous fat and softer tissue layers which are more prone to deformation.
Interestingly, in the chest region (RUT), the measured amplitude remained relatively consistent when the tag was placed on clothing (11.6 mm) and when it was mounted on an elastic belt over the clothing (12.1 mm), as shown in Figure 3.17a. This may be explained by the structural rigidity of the chest, which is supported by the rib cage and pectoral muscles, and female subject worn bra strap, providing a more stable and consistent dielectric interface. However, such a difference caused by additional insulation was not guaranteed in all subjects or positions, likely due to the radiation difference of commercial tag samples.

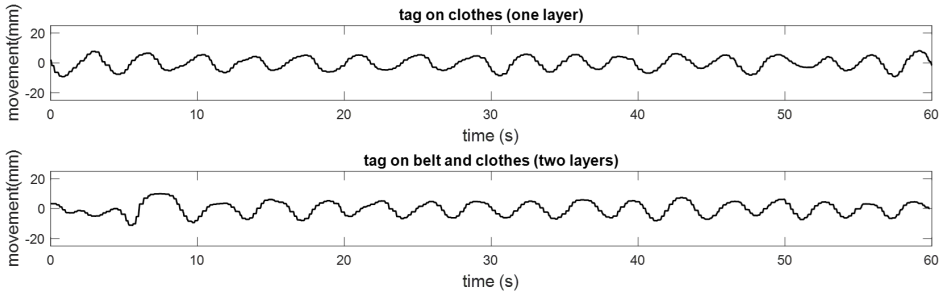

(a) Put tag on chest clothing or on belt over clothing

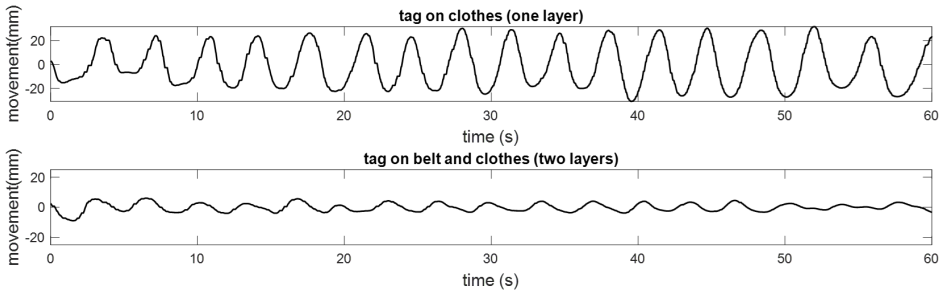

(b) Put tag on abdomen clothing or on belt over clothing

Figure 3.17: Effects of different insulation between tag and skin on chest and abdomen

3.2.3 Validation of RFID Tag Configurations with PZT Reference

This subsection presents a detailed validation of various RFID tag configurations using a synchronized PZT belt as a reference. Both two-tag and four-tag placements were evaluated on the chest and abdomen to examine spatial symmetry, signal consistency, and respiratory cycles alignment with PZT belt.
The PZT belt signal is shown in Figure 3.18, which exhibit a clear one-to-one correspondence with the respiratory cycles, making them a reliable "ground truth" reference for validating the target system's output.

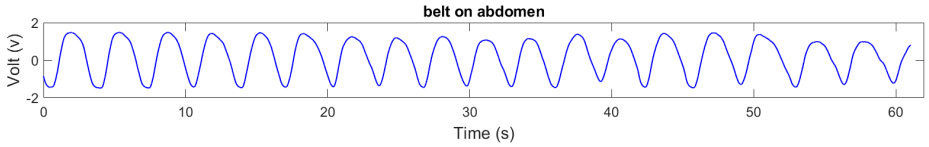

Figure 3.18: PZT belt signal

To evaluate the accuracy of the RFID tag system, correlation was calculated between tags and the piezoelectric (PZT) belt when collocated on the same body region (chest or abdomen) under multiple tag configurations. Note that all signals were normalized in amplitude prior to comparison with the PZT reference, and thus only waveform consistency and temporal alignment were evaluated.

Representative examples of aligned waveforms under the 2-tag (chest–abdomen) configuration are shown in Figure 3.19, illustrating the general agreement between RFID and belt measurements. For comprehensive evaluation, the results from all experimental settings are summarized in Table 3.1, which lists respiratory rate estimates and maximum cross-correlation (Max CC) relative to the PZT belt.

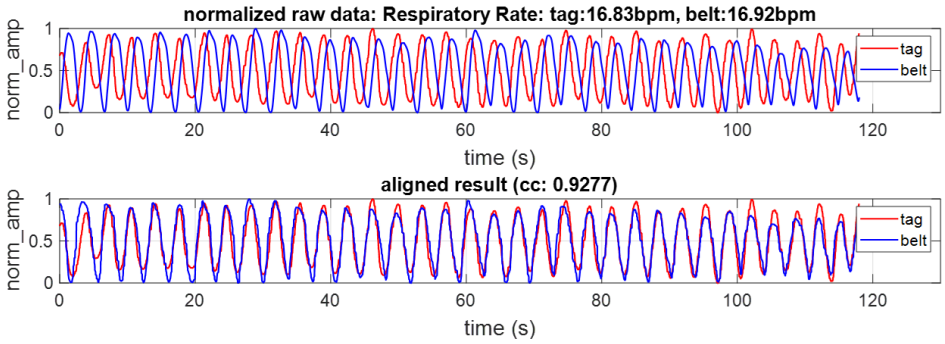

Figure 3.19: Results of PZT validation under setting in Figure 3.5a

.

Table 3.1: Respiratory rate and cross-correlation under different tag settings

Setting	**Location**	**Resp. Rate (bpm)**		**Cross-Corr.**
		RFID	**Belt**	
2-tag	Upper Chest	17.87	17.82	0.8824
	Midline Abdomen	16.83	16.92	0.9277
2-tag (bilateral)	Chest – RUT	17.00	17.39	0.8758
	Chest – LUT	17.00		0.8691
	Abdomen – RA	15.89	15.90	0.9153
	Abdomen – LA	15.89		0.9215
4-tag	RUT	12.76	15.33	0.3156
	LUT	11.77		0.2821
	RA	14.21	15.77	0.7405
	LA	14.21		0.6934

The experiments demonstrate that RFID tags achieve high alignment and frequency accuracy when placed in the same region as the belt sensor under 2-tag setups with all correlations exceeding 0.86, with maximum cross-correlation exceeding 0.92 and frequency errors below 0.1 bpm, indicating strong consistency across different tag placements and body regions.
RFID tags demonstrated good bilateral symmetry and consistent respiratory sensing on both the chest and abdomen with minimal side-to-side variance, although the alignment performance on the chest was slightly lower than that on the abdomen, possibly due to the smaller motion amplitude of the thoracic cavity during

breathing. These results demonstrate that the RFID-based system provides reliable measurements of the respiratory cycle, supporting its potential as an effective non-contact method for respiratory monitoring.
However, under four-tag configurations, abdominal signals remained relatively stable but showed decreased accuracy and chest signals were more severely affected, likely due to increased signal overlap and tag-to-tag interference.

4

Tag Antenna Design

We explored the feasibility of using commercial RFID tags for respiration monitoring in chapter 3. However, experimental results revealed that when placed directly on human skin, the tags often failed to operate reliably. This issue is primarily due to the high dielectric losses and permittivity of human tissue, which significantly detune the tag antenna and degrade its performance. To overcome this limitation, this chapter focuses on the design and simulation of a customized UHF RFID tag antenna. The goal is to optimize the antenna structure for on-skin operation, minimizing performance degradation caused by proximity to the body. This enables more stable and reliable signal acquisition for continuous respiration monitoring.

4.1 Antenna Design and Simulation

During the antenna design, we first conducted a comprehensive investigation and comparison of several commercially available RFID tags, focusing on key parameters such as small size, high scalability, moderate read range. Based on these evaluations, the AD Bling R6 tag which is from Avery company[36] was selected as the baseline antenna design. This tag is originally designed for jewelry and cosmetics applications, featured a compact size and good adhesion properties. One of the key reasons for selecting this tag is its meandered antenna structure, which allows for effective miniaturization without significantly compromising performance. The meander geometry enables the antenna to achieve a relatively long electrical length within a limited physical area, which is advantageous for compact wearable designs[37]. However, while the original design performs well in free-space conditions, its antenna geometry is not optimized for on-body environments, where dielectric loading and detuning effects can significantly degrade performance. This limitation is particularly important for wearable respiratory monitoring applications, which require stable performance in close proximity to the human body. Therefore, this tag antenna served as a starting point for further optimization to suit on-body operation. To address this limitation, we refined the antenna's geometric parameters with the objective of maximizing its performance under on-skin conditions. Another antenna shape is inspired by a previously proposed antenna design optimized for sensing physiological parameters of the human body (temperature, pressure, heartbeat, etc.), therefore, it has been optimized by human tissue simulation and can perform well on human body[27].
To accurately assess and optimize the antenna performance, CST Microwave Studio was employed to perform detailed electromagnetic simulations, in which multilayer

human tissue models were incorporated, including skin, fat, and muscle. These simulations were used to evaluate the antenna's impedance matching, resonant frequency shifts, and radiation characteristics in realistic body-mounted scenarios. Both antenna designs share identical environmental parameters to ensure consistent comparative analyses and reliable performance assessments.

4.1.1 Antenna Geometry Designs

4.1.1.1 Meander Antenna Design

We adjusted the specific geometric values based on this meander antenna pattern, to enhance the performance under body loading conditions. Figure 4.1 shows the geometry of meander antenna, table 4.1 illustrates the parameters of meander antenna.

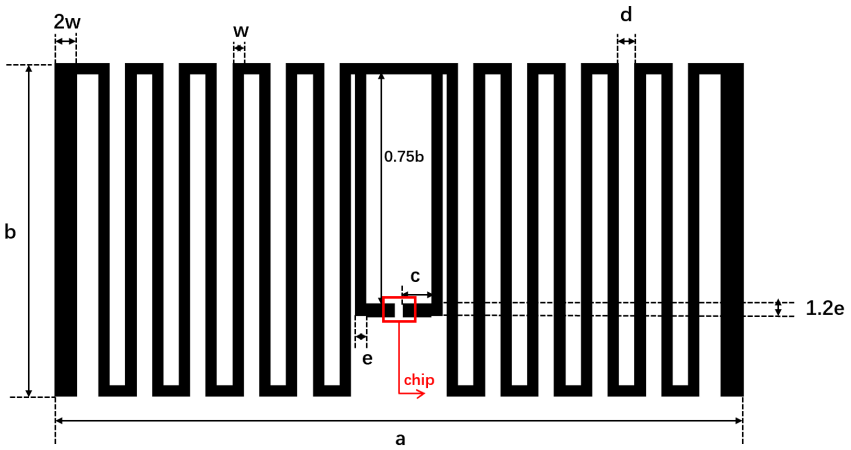

Figure 4.1: Geometry and key dimensions of the modified meander-line tag antenna.

Table 4.1: Geometry parameters of the Loaded Meander Tag Antenna (mm)

Parameters	a	b	c	d	e	t_c	t_s	w
Values	36	17.4	0.5	1.4	0.6	0.018	0.5	0.6

4.1.1.2 Doubleloop Antenna Design

The second antenna geometry draws upon previously published designs optimized for on-body physiological monitoring applications [27]. To better suit the requirements of our respiratory monitoring scenario, the original structure was adapted by adjusting both the shape and key geometric parameters to achieve improved impedance matching and stable electromagnetic performance when placed near human tissue. Figure 4.2 shows the geometry of doubleloop antenna and optimized parameters of doubleloop antenna.

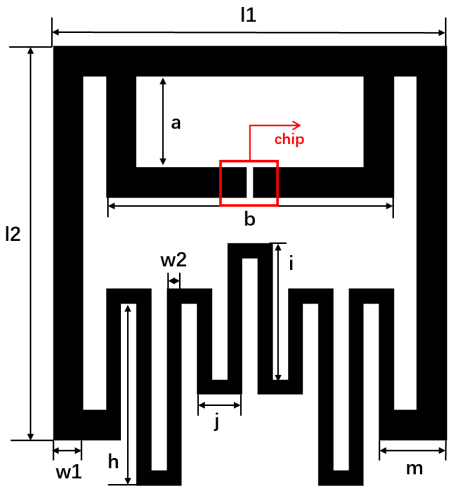

Parameter	Value (mm)
a	5.4
b	17.1
j	2.7
h	10.8
i	8.1
l_1	23.4
l_2	23.4
m	4.05
t_s	0.6
w_1	1.8
w_2	0.9

Figure 4.2: Geometry and key parameters of the double-loop tag antenna

4.1.1.3 Simple Double-loop Antenna Design

Based on the original double-loop geometry, the antenna was further modified to improve structural simplicity and symmetry. In particular, the T-match section around the chip connection was redesigned into a more balanced configuration, ensuring equal current paths on both sides of the feed. At the same time, the lower part of the antenna was simplified by adopting a symmetric folded-line structure, replacing the more intricate features of the original design. These modifications result in a compact and symmetric layout, which not only facilitates easier manual fabrication but also maintains stable impedance characteristics suitable for on-body UHF RFID operation. The geometry and detailed parameters of the simple antenna are shown in figure 4.3.

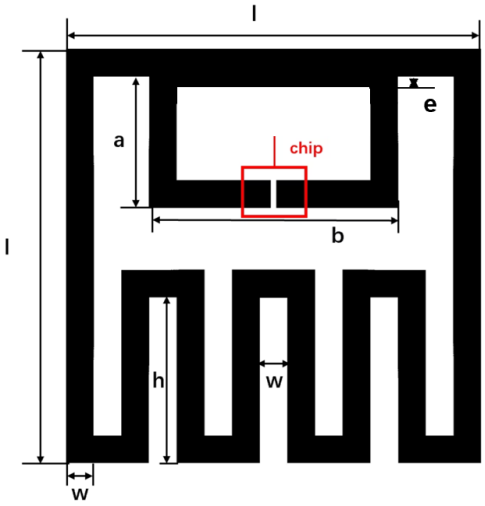

Parameter	Value (mm)
l	30
a	9.5
b	18
w	2
h	12
e	0.7

Figure 4.3: Geometry and key parameters of the simple double-loop tag antenna

4.1.2 Environmental Setting in CST

In CST, we simulated the scenario where the RFID tag is placed on human body. A three-layer human tissue model consisting of skin, fat, and muscle was defined, the final antenna design and simulation are shown in figure 4.4. Both antenna designs utilized identical environmental parameters to ensure fair comparisons, as listed in Appendix Table A.1.

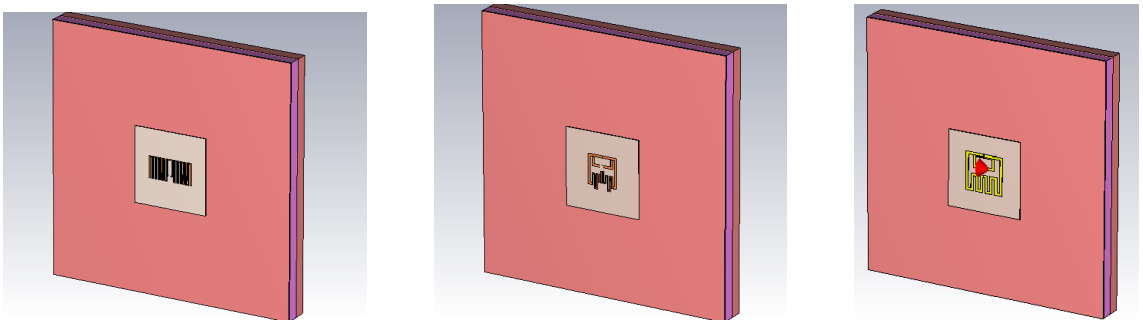

(a) Meander antenna simulation design

(b) Double-loop antenna design

(c) Simple Double-loop antenna design

Figure 4.4: Three antenna design simulations in CST

4.1.3 Antenna Simulation

In the CST simulations, a discrete port with a characteristic impedance of 50 Ohm was used to represent the chip connection, simplifying the modeling process and improving simulation efficiency. After the simulations were completed, the s1p files were exported.
However, the actual RFID chip impedance is not 50 Ohm, which means the simulated S11 values do not directly reflect the true reflection behavior between the antenna and the real chip. Therefore, it is necessary to post-process the simulation results to account for the actual complex chip impedance. MATLAB is subsequently used to evaluate the impedance matching performance between the simulated antenna and the real RFID chip, providing a more accurate representation of the reflection coefficient and impedance matching condition. In MATLAB, the antenna impedance is first calculated from the simulated S_{11} data using the following transformation:

$$Z_{\text{ant}} = Z_0 \cdot \frac{1 + S_{11}}{1 - S_{11}} \tag{4.1}$$

where $Z_0 = 50$ Ohm is the reference impedance used in CST simulations, and S_{11} is the reflection coefficient exported from the s1p file.
Next, the actual impedance characteristics of the RFID chip is calculated using its real resistance and capacitance parameters. The chip impedance in RC parallel circuit[38] was modeled as[39]:

$$Z_{\text{chip}}(f) = \frac{1}{\frac{1}{R} + j\omega C_p} \tag{4.2}$$

. To evaluate the actual matching performance between the antenna and chip, we compute the reflection coefficient at the antenna-chip interface as:

$$\Gamma_{\text{chip}} = \frac{Z_{\text{chip}} - \overline{Z_{\text{ant}}}}{Z_{\text{chip}} + Z_{\text{ant}}} \tag{4.3}$$

The chips we used are specified according to the information provided by Impinj [38]. The capacitance and resistance values for the two types of chips can be found in Table 4.2 and Table 4.3 respectively. Our operating frequency is 868 MHz, which allows us to calculate the complex impedance of the chip. Based on the antenna impedance obtained from CST simulations, we can calculate the reflection coefficient of the antenna when the chip is mounted. This enables us to estimate the potential losses due to impedance mismatch.

Table 4.2: Monza R6-P Enduro Chip Port Parameters (used for meander antenna)

Parameter	**Typical Value**	**Comments**
C_p	1.44 pF	Chip capacitance, including Enduro pads.
R_p	1.2 kΩ	Chip resistance.

Table 4.3: Monza R6-P Non-Enduro Chip Port Parameters (used for double-loop antenna)

Parameter	**Typical Value**	**Comments**
C_p	1.13 pF	Chip capacitance, excluding Enduro pads.
R_p	1.2 kΩ	Chip resistance.

4.1.3.1 Design 1: Meander-Line Antenna

Impedance Matching

The meander antenna impedance is shown in figure 4.5, at the 868 MHz, the simulated antenna impedance is $Z_{\text{ant}} = 14.76 + j127.28\ \Omega$, while the chip impedance is $Z_{\text{chip}} = 13.36 - j125.91\ \Omega$. Ideally, for optimal power transfer, the antenna impedance should be the complex conjugate of the chip impedance. Therefore, the results indicates a good impedance match. This suggests that the designed antenna is well-tuned to the chip at 868 MHz, which helps minimize reflection and maximize the power delivered to the chip.

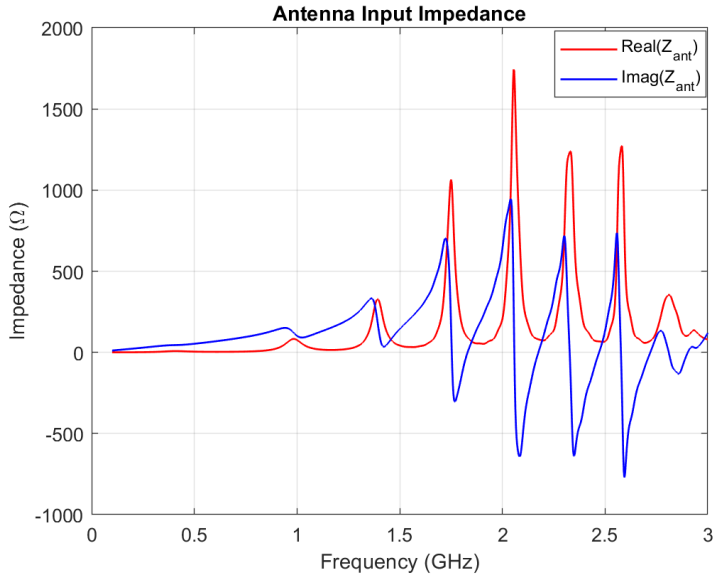

Figure 4.5: Impedance matching of Meander Antenna

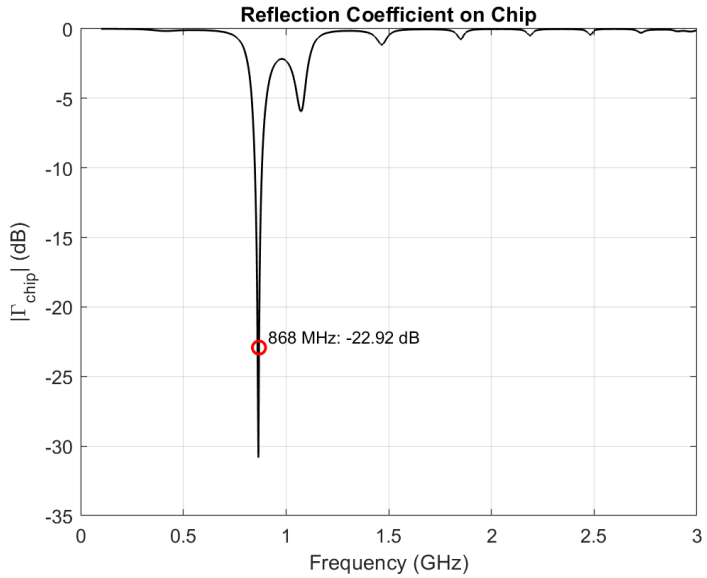

Figure 4.6: Reflection coefficient (S_{11}) of Meander Antenna Design.

Figure 4.6 shows the reflection coefficient (S_{11}) of the loaded meander-line antenna. The resonance point is observed near 868 MHz, with S_{11} below -10 dB. Table 4.4 shows the detailed performance results: The antenna exhibits a resonant frequency of 865.60 MHz, which is close to the target UHF RFID band (around 868 MHz), indicating effective frequency tuning. The minimum reflection coefficient $|\Gamma|$ reaches -30.83 dB at resonance, signifying excellent impedance matching and minimal power reflection. The -10 dB bandwidth spans 34.45 MHz, providing sufficient tolerance for slight detuning effects due to fabrication error or human loading. The wider -3 dB bandwidth of 112.71 MHz further confirms the antenna's ability to maintain good

performance across a broad frequency range. Overall, these results demonstrate that the proposed design achieves both effective resonance and robust matching within the intended operating band, making it a promising candidate for body-worn UHF RFID applications.

Table 4.4: Meander Antenna Performance Parameters (Design 1)

Parameter	**Value**
Resonant frequency	865.60 MHz
Minimum $\|\Gamma\|$ (Reflection coefficient)	-30.83 dB
-3 dB bandwidth	112.71 MHz (819.12–931.82 MHz)
-10 dB bandwidth	34.45 MHz (848.39–882.84 MHz)

Radiation Pattern

Figure 4.7 shows the 3D far-field radiation pattern of the meander-line antenna, where the main lobe directionality and spatial energy distribution can be clearly observed. To further analyze the antenna's behavior in principal planes, figure 4.8 presents the 2D radiation patterns of the meander-line antenna at 860 MHz in the $\phi = 0°$ (E-plane) and $\phi = 90°$ (H-plane). In the E-plane, the main lobe gain ($\phi = 0°$) is -23.7 dBi with a broad beamwidth of 180°, indicating an omnidirectional pattern but weak radiation strength. In contrast, the H-plane ($\phi = 90°$) exhibits a higher main lobe gain of -8.78 dBi, a more focused beam (3 dB beamwidth of 10.4°), and good sidelobe suppression, demonstrating a directional radiation characteristic. However, the overall gain remains low, suggesting moderate performance.

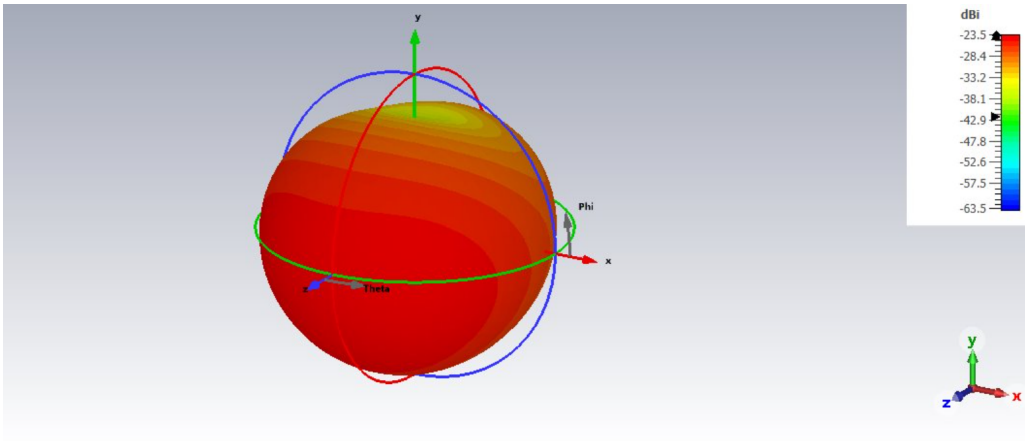

Figure 4.7: 3D Radiation pattern of Meander Antenna

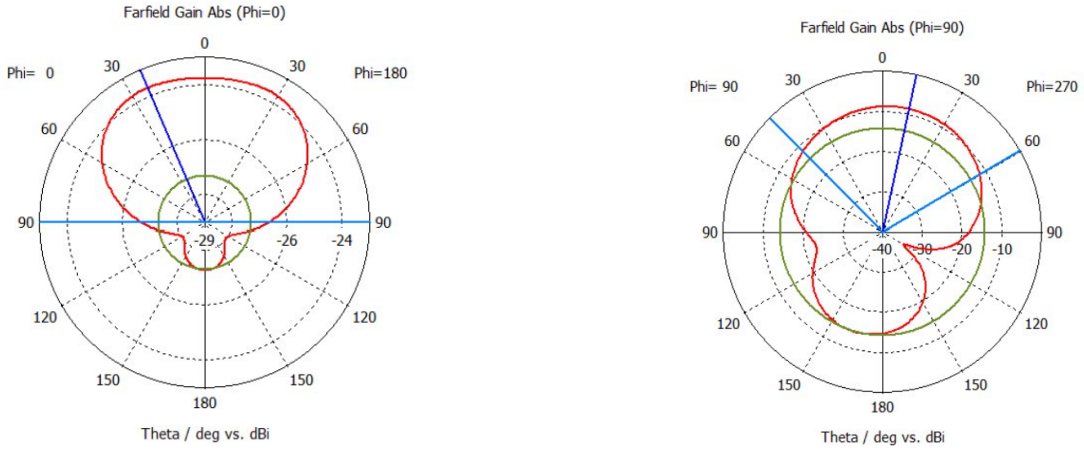

(a) E-plane ($\phi = 0°$) **(b)** H-plane ($\phi = 90°$)

Figure 4.8: 2D polar radiation patterns of meander antenna in two orthogonal planes.

4.1.3.2 Design 2: Double-loop Antenna

Impedance Matching

The doubleloop antenna impedance is shown in figure 4.9. At 868 MHz, the simulated impedance of the double loop antenna is $Z_{ant} = 19.00 + j162.61\ \Omega$, while the selected doubleloop antenna chip impedance is $Z_{chip} = 21.55 - j159.35\ \Omega$. This indicates that the antenna and chip are nearly complex conjugate pairs, which is the ideal condition for maximum power transfer. Although a small mismatch exists in both real and imaginary parts, the values are sufficiently close to ensure efficient impedance matching. This is further supported by the following low reflection coefficient ($|\Gamma| = -21.27$ dB) observed at resonance, confirming that the antenna is well-matched to the chip at the operating frequency. Such matching contributes to minimal power loss and improved read range performance.

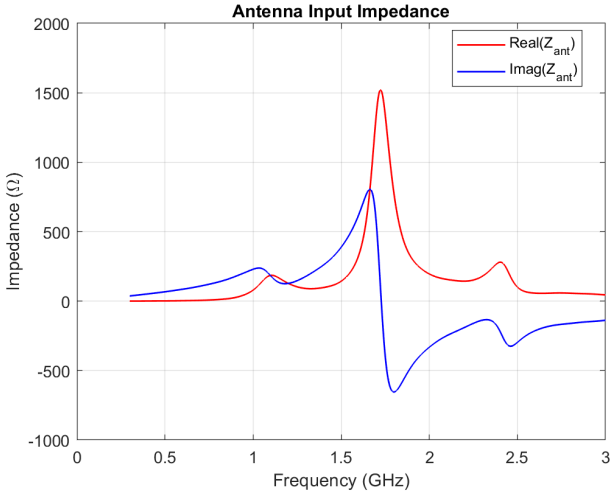

Figure 4.9: Impedance matching of Doubleloop Antenna.

Figure 4.10 shows the S_{11} parameter of the doubleloop antenna design. Table 4.5 summarizes the detailed performance parameters of the doubleloop antenna. The antenna exhibits a resonant frequency of 864.30 MHz, which is very close to the target 868 MHz operating frequency, indicating good frequency tuning. The minimum reflection coefficient $|\Gamma|$ reaches -21.27 dB, suggesting excellent impedance matching and minimal power reflection. The antenna demonstrates a wide -3 dB bandwidth of 131.89 MHz, ensuring robust performance across a broad frequency range. Additionally, the -10 dB bandwidth is 40.11 MHz (844.62–884.73 MHz), covering the entire European UHF RFID band (865–868 MHz), making the antenna suitable for practical RFID applications. Overall, the doubleloop antenna shows good resonance, strong impedance matching, and adequate bandwidth characteristics.

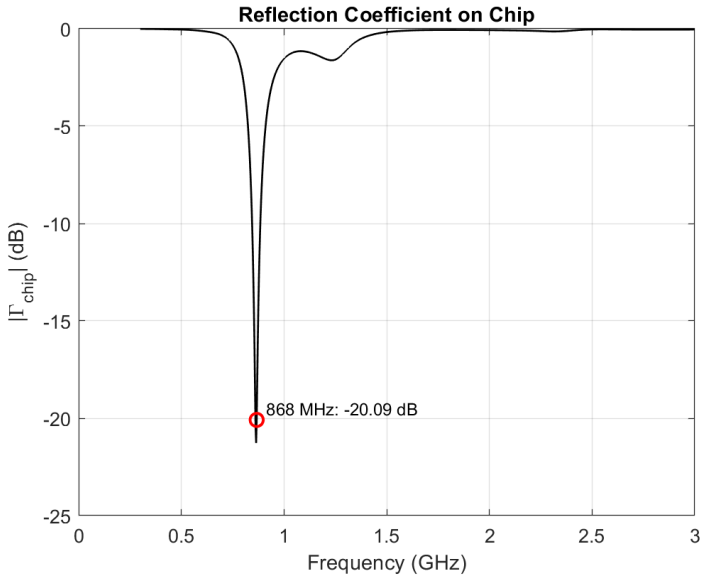

Figure 4.10: Reflection coefficient (S_{11}) of Doubleloop Antenna Design.

Table 4.5: Doubleloop Antenna Performance Parameters (Design 2)

Parameter	**Value**
Resonant frequency	864.30 MHz
Minimum $\|\Gamma\|$ (Reflection coefficient)	-21.27 dB
-3 dB bandwidth	131.89 MHz (806.57–938.46 MHz)
-10 dB bandwidth	40.11 MHz (844.62–884.73 MHz)

Radiation Pattern

Figure 4.11 shows the 3D far-field radiation pattern of the doubleloop antenna. Figure 4.12 shows the 2D far-field radiation patterns of the double-loop antenna in the E-plane ($\phi = 0°$) and H-plane ($\phi = 90°$) at 868 MHz. In the E-plane, the antenna exhibits a broad omnidirectional pattern with a maximum gain of -15.5 dBi and a 3 dB beamwidth of 198.7°, indicating excellent coverage capabilities suitable

for wireless communication applications. The side lobe level of -3.8 dB suggests acceptable pattern quality with minimal interference potential. Conversely, the H-plane shows a more directional characteristic with a narrower 3-dB beamwidth of 95.8° while maintaining the same peak gain, though with elevated side lobe levels of -1.4 dB. This asymmetry between the two principal planes is attributed to the antenna's geometric structure and ground plane effects, resulting in a radiation pattern that provides a good compromise between omnidirectional coverage and moderate directivity. Overall, the doubleloop antenna indicate a maximum gain of approximately −18 dBi, which is considered significantly low for practical RFID applications. This poor radiation performance may be attributed to the compact structure and loop geometry, it might result in destructive interference and limited current distribution, impairing far-field radiation efficiency.

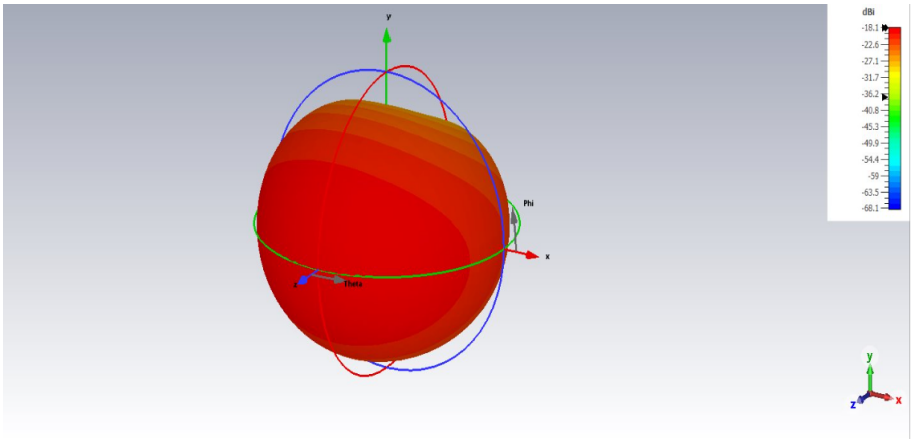

Figure 4.11: Radiation pattern of Doubleloop Antenna.

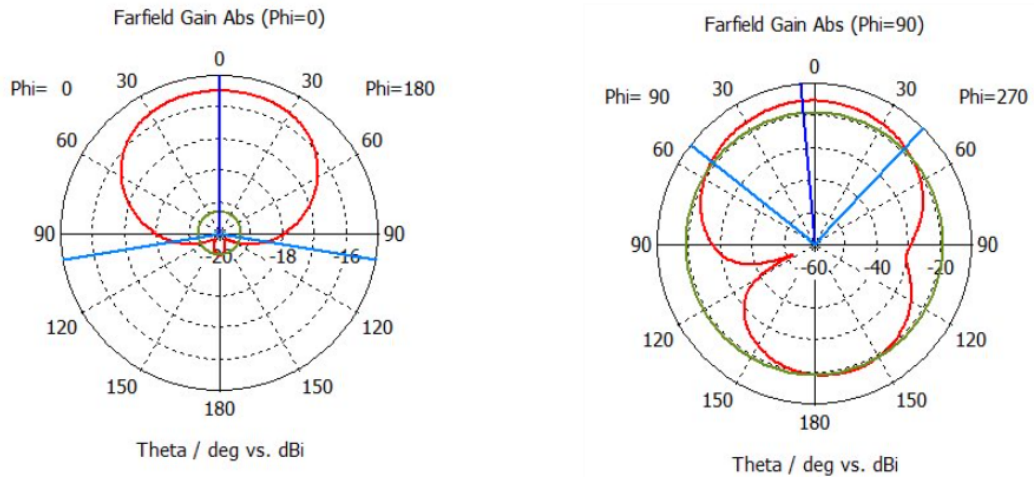

(a) Radiation pattern in E-plane ($\phi = 0°$)

(b) Radiation pattern in H-plane ($\phi = 90°$)

Figure 4.12: 2D polar radiation patterns of doubleloop antenna in two orthogonal planes.

4.1.3.3 Design 3: Simple Double-loop Antenna

Impedance Matching

The simple doubleloop antenna impedance is shown in figure 4.13. At 868 MHz, the simulated impedance of the double loop antenna is $Z_{ant} = 17.42 + j160.33\ \Omega$, while the selected doubleloop antenna chip impedance is $Z_{chip} = 21.55 - j159.35\ \Omega$. The antenna and chip impedances at 868 MHz are very close, nearly achieving conjugate matching. This indicates that the double-loop antenna is well matched to the chip at the target frequency, ensuring high energy transfer efficiency.

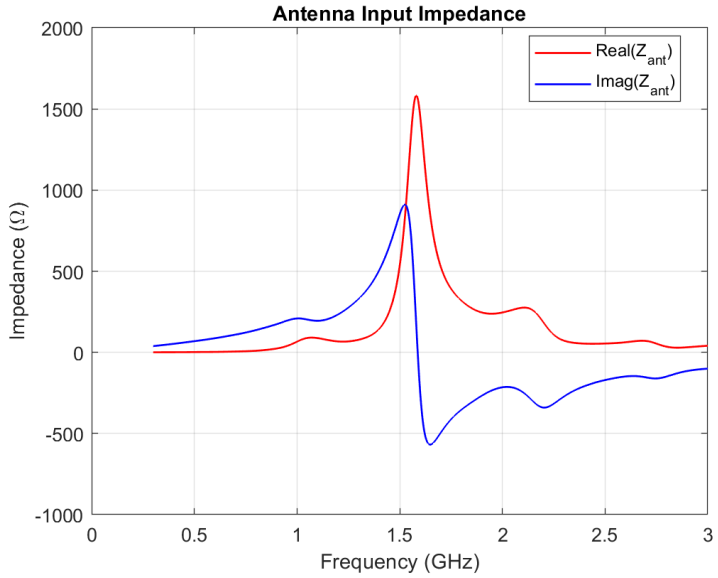

Figure 4.13: Impedance matching of Simple Doubleloop Antenna.

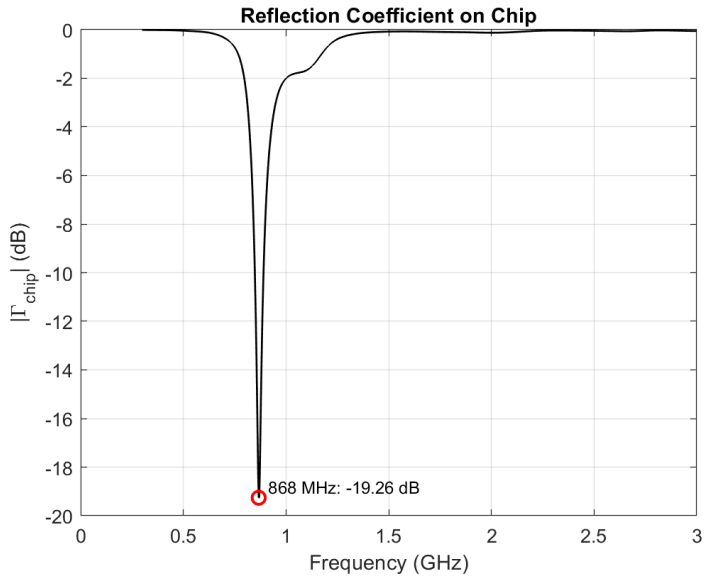

Figure 4.14: Reflection coefficient (S_{11}) of simple Doubleloop Antenna Design.

Figure 4.14 shows the reflection coefficient of the simple doubleloop antenna and Table 4.6 summarizes the key performance parameters of the antenna. The simple doubleloop antenna utilizes the Monza R6-P non-Enduro Chip. Simulation results show that the simple double-loop antenna resonates at 867 MHz, which is only 1 MHz away from the target frequency of 868 MHz, indicating excellent frequency alignment. The minimum reflection coefficient is −19.26 dB, the chip and antenna have achieved approximate conjugate matching. The −10 dB bandwidth of 42.22 MHz and −3 dB bandwidth of 138.75 MHz fully covers the UHF RFID band while providing tolerance for possible detuning in practical environments. Overall, the design provides deep matching, high efficiency, and sufficient bandwidth at 868 MHz, which ensures strong potential for long read ranges.

Table 4.6: Simple Doubleloop Antenna Performance Parameters (Design 3)

Parameter	**Value**
Resonant frequency	867.00 MHz
Minimum $\|\Gamma\|$ (Reflection coefficient)	−19.26 dB
−3 dB bandwidth	138.75 MHz (811.21–950.07 MHz)
−10 dB bandwidth	42.22 MHz (848.31–890.53 MHz)

Radiation Pattern

Figure 4.15 shows the 3D far-field radiation pattern of the simple doubleloop antenna. Figure 4.16 shows the 2D gain radiation patterns of the simplified doubleloop antenna at 868 MHz. It can be observed that the antenna maintains acceptable radiation performance in both principal planes ($\phi = 0°$ and $\phi = 90°$). The main lobe directions are close to the vertical axis, and the beamwidths are relatively wide, at 206.7° and 94.7°, respectively, indicating good coverage characteristics. The peak gain is approximately −13.2 dBi.

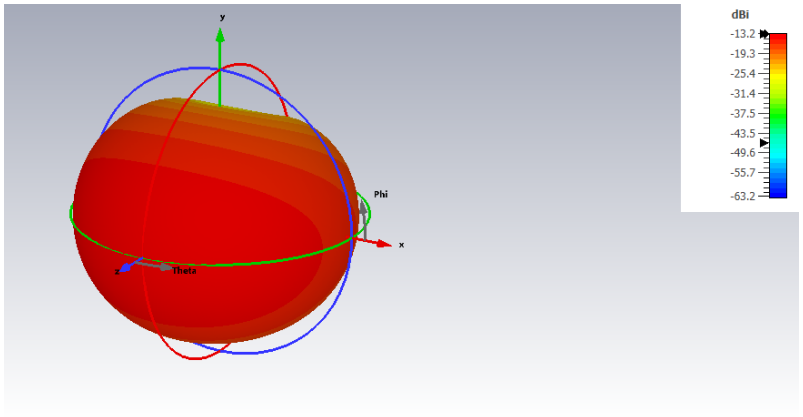

Figure 4.15: Radiation pattern of Simple Doubleloop Antenna.

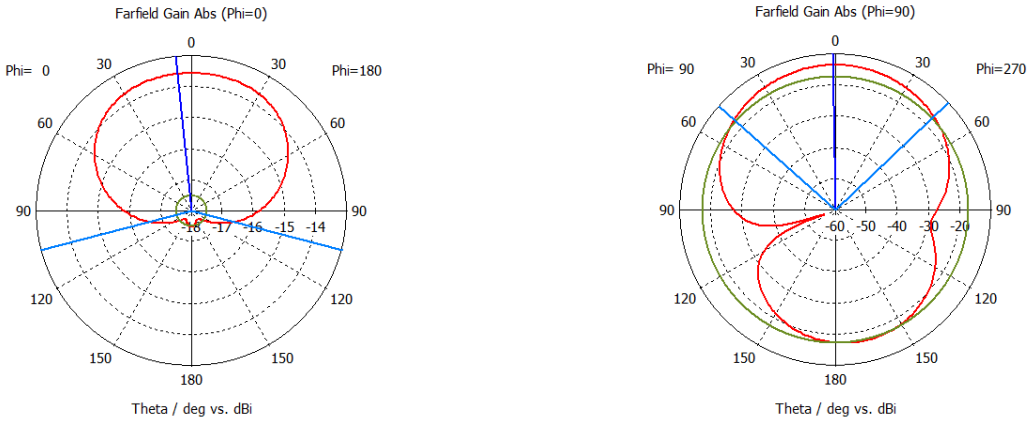

(a) E-plane ($\phi = 0°$) **(b)** H-plane ($\phi = 90°$)

Figure 4.16: 2D polar radiation patterns of simple doubleloop antenna in two orthogonal planes.

4.2 Fabrication and Evaluation of the Flexible Antenna Prototype

Following the completion of the antenna design, we proceeded with the physical fabrication and experimental validation of the antenna. Considering the difficulty and cost of the manufacturing process, we choose to use doubleloop antenna, we implemented two different fabrication methods for the antenna and subsequently assessed the performance of the prototypes using a vector network analyzer.

4.2.1 Manufacturing of the antenna

4.2.1.1 Method 1: Conductive silver adhesive deposition through stencil

The antenna is intended for on-skin respiratory monitoring, the substrate material must be highly flexible, soft, and biocompatible to ensure conformal contact with human skin and minimize discomfort during long-term wear. PDMS (Polydimethylsiloxane) meets these criteria due to its excellent mechanical flexibility, chemical stability, and skin-friendliness, making it a widely adopted substrate in wearable biomedical devices[40].
For the antenna conductor, silver conductive adhesive was selected as the antenna material due to its unique suitability for flexible and skin-integrated applications. Unlike traditional metallic conductors that require high-temperature and long-time processing, silver conductive adhesive can be deposited at 100°, which is critical for maintaining the mechanical integrity of soft substrate PDMS. Moreover, it offers sufficient electrical conductivity in the UHF band, while its viscoelastic nature enhances adhesion and mechanical compatibility with stretchable or deformable surfaces. These properties are particularly advantageous for wearable antennas used in respiratory monitoring, where close skin contact and long-term comfort are essential. Additionally, its low cost and compatibility with stencil-based patterning methods

further support rapid prototyping[41].
Based on the designed antenna pattern, a custom stencil was manufactured(is shown in figure 4.17a). We first fabricated the PDMS substrate, the base agent and curing agent (Sylgard 184, Dow Corning) were weighed and mixed at a 10:1 ratio by weight. The mixture was thoroughly stirred using a glass rod, during which numerous microbubbles were introduced. The viscous mixture was then poured into a dish to form a thin layer and left undisturbed for degassing at room temperature (or placed in a vacuum desiccator if available). Subsequently, the sample was thermally cured in a 70°C oven for 1.5-2 hours. After curing, the PDMS layer was carefully peeled off and trimmed to the desired dimensions. After the PDMS implementation, we do the antenna fabrication process, the stencil was first placed precisely onto the surface of the flexible PDMS substrate. The silver conductive adhesive was then applied uniformly over the stencil(is shown in figure 4.17b); the adhesive penetrated through the stencil's apertures corresponding to the antenna pattern and deposited onto the substrate surface, thereby forming the pre-designed antenna geometry(is shown in figure 4.18). After the conductive adhesive cured (70°, 1h), a final flexible antenna prototype was obtained.

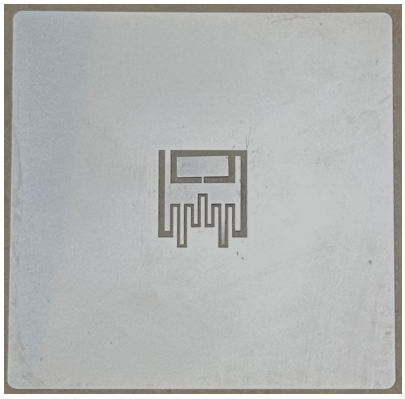

(a) Doubleloop antenna stencil

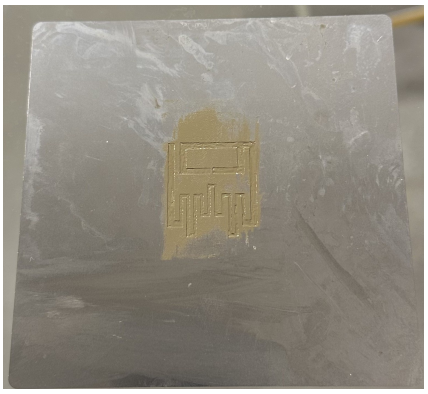

(b) Apply silver glue to the stencil

Figure 4.17: Fabrication process of the doubleloop antenna using stencil printing.

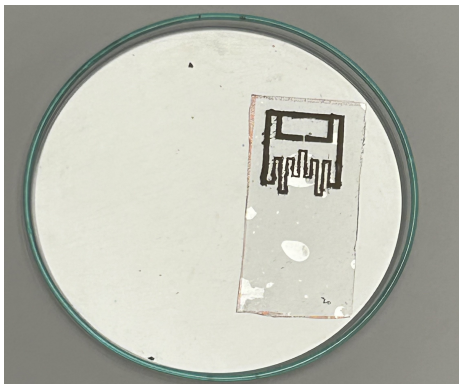

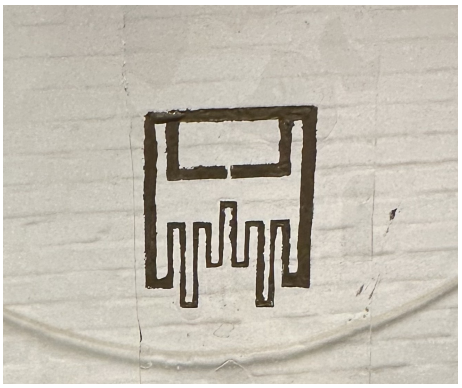

Figure 4.18: Antenna pattern obtained

4.2.1.2 Method 2: Copper tape engraving

The antenna pattern was manually engraved onto the copper surface, according to the simple antenna pattern and parameters, we manually engraved the antenna pattern on the copper tape with a small needle, the final result of the manually crafted antenna is shown in figure 4.19.

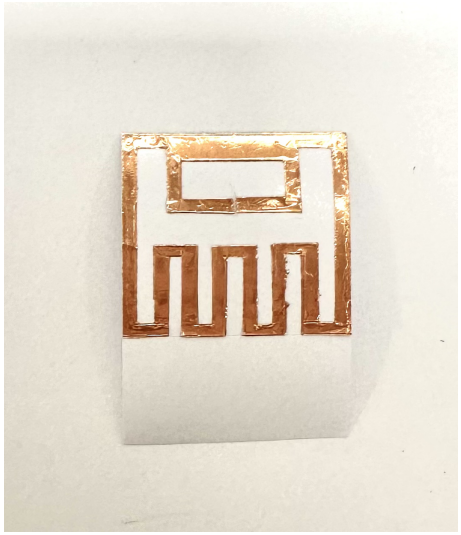

Figure 4.19: Apply adhesive copper tape as antenna

4.2.2 Performance evaluation of the antenna

A vector network analyzer (VNA) was employed to evaluate the performance of the fabricated flexible antenna prototype. The VNA(is shown in figure 4.20) was configured with a start frequency of 100 MHz and a stop frequency of 5 GHz, using a bandwidth of 1 kHz and a frequency step size of 980 kHz, resulting in a total of 5000 sampling points.
During the measurement, an SMA handheld probe was used to contact the antenna feed terminals located at the chip gap, ensuring reliable electrical connection at both ends of the antenna. The reflection coefficient (S_{11}) was recorded from the VNA, and the corresponding data were post-processed in MATLAB to calculate the input impedance of the antenna over the measured frequency range.
To ensure consistency with the simulation environment used in CST, the antenna was placed directly on the skin surface during testing, as shown in Figure 4.21. This placement replicates the realistic electromagnetic conditions experienced in practical applications and allows for a more accurate comparison between the measured and simulated results.

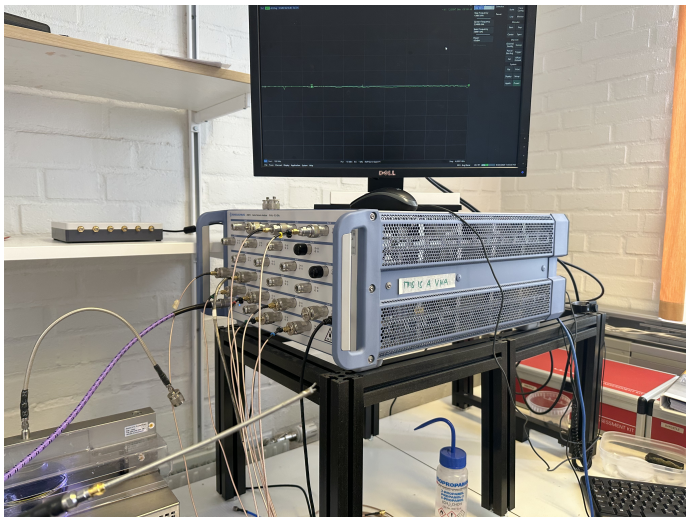

Figure 4.20: The vector network analyzer

(a) Use SMA to test the copper tape antenna

(b) Use SMA to test the stencil printing antenna

Figure 4.21: Evaluation of the antenna

Measured performance of the antenna prototype

To evaluate the performance of our designed antenna, we measured the input impedance of two RFID tag antennas fabricated using different methods: Conductive silver adhesive deposition by using stencil and Engraving by hand on copper tape. The impedance measurements were conducted using a calibrated Vector Network Analyzer (VNA), and the results were processed in MATLAB to extract the real and imaginary parts of the antenna input impedance across a frequency range of 0.1-5 GHz.
Figure 4.22 shows the impedance characteristics of the copper-fabricated antenna. At 868 MHz, the input impedance is significantly mismatched, with a real part

of approximately 22.35 Ohm and an imaginary part of -194.79 Ohm, indicating a strong capacitive behavior and poor impedance matching.
In contrast, the silver paste antenna, shown in Figure 4.23, exhibits an input impedance of 2.39 Ohm (real) and -161.87 Ohm (imaginary) at 868 MHz. Although this still indicates poor matching at the target frequency, a resonant behavior is observed near 653 MHz with an S11 of approximately -11 dB, suggesting partial impedance matching in the lower UHF band.
These results highlight that the antenna impedance characteristics is significantly affected by fabrication material, likely due to differences in surface roughness, conductivity, and fabrication uniformity.

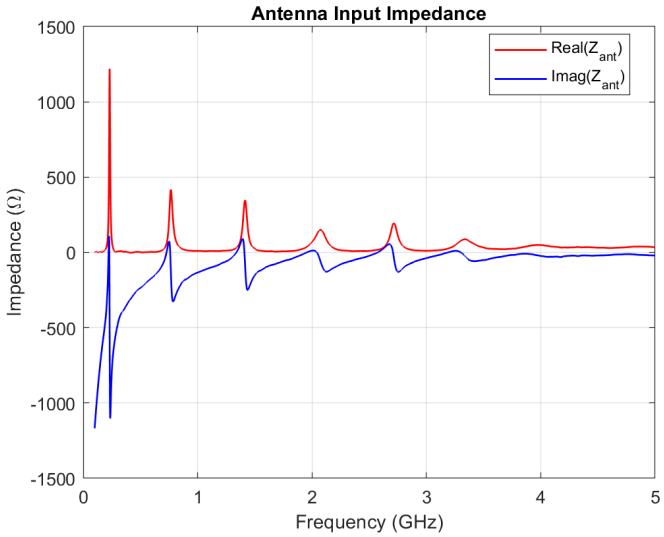

Figure 4.22: Impedance matching of Doubleloop Antenna prototype(copper tape).

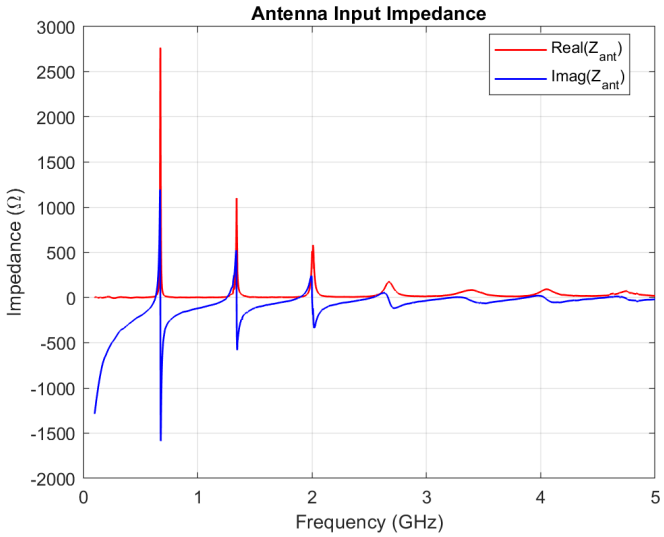

Figure 4.23: Impedance matching of Doubleloop Antenna prototype(silver paste).

5

Discussion

5.1 Results Analysis

Experimental results show that RFID tags can accurately reflect the periodicity of respiration. Under normal breathing conditions, the waveforms extracted by the system exhibit good temporal consistency with the reference signals obtained from the PZT belt. However, several issues still remain.

Amplitude Differences(RFID vs. PZT)

In the experiments, a PZT belt was employed as the reference signal. However, it is important to note that the physical quantities measured by the PZT sensor and the RFID system are fundamentally different. The PZT sensor primarily responds to local mechanical stress and strain variations associated with respiration, rather than measuring radial displacement at a specific region [34]. This is particularly relevant in the chest, where lateral expansion of the rib cage contributes significantly to chest wall movement [35]. In contrast, the RFID system is sensitive to the spatial displacement of the tag relative to the reader antenna. While PZT sensors capture composite mechanical deformation of the body surface, RFID systems typically measure geometric distance changes, and are more sensitive to directional displacement. Consequently, the amplitude outputs of the two systems are not directly comparable in a quantitative sense, and in our work the PZT belt was only used for validating respiratory phase and cycle consistency, rather than displacement magnitude.
Despite this limitation, analysis of raw RFID displacement signals provides valuable insight into regional breathing mechanics. RFID measurements revealed a consistent and physiologically meaningful trend: abdominal tags exhibited greater displacement amplitudes than chest tags. For example in Figure 5.1, abdominal recordings showed average displacements around 30 mm, whereas chest recordings were 8.5 mm. This result is consistent with known biomechanics of quiet respiration, where abdominal expansion contributes more prominently to anterior–posterior motion compared to thoracic motion. The PZT reference signals qualitatively corroborated this trend, with abdominal placements producing higher voltage amplitudes than chest placements (e.g., 1.51 V vs. 0.97 V).

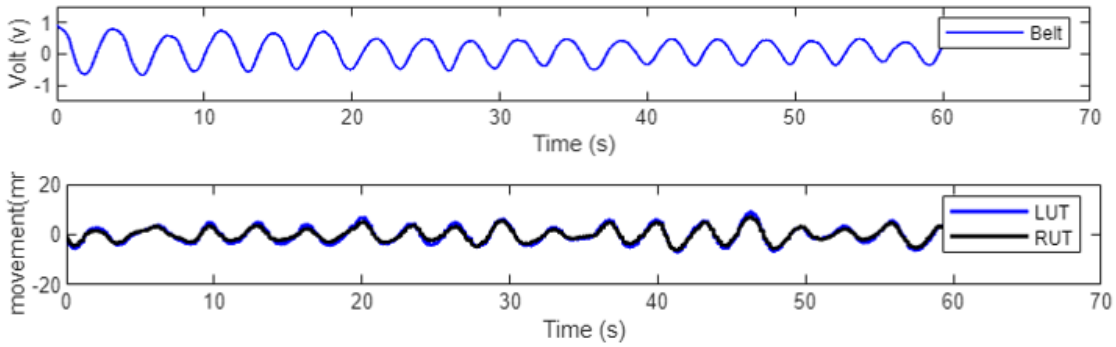

(a) Chest belt and RFID signal during breathing

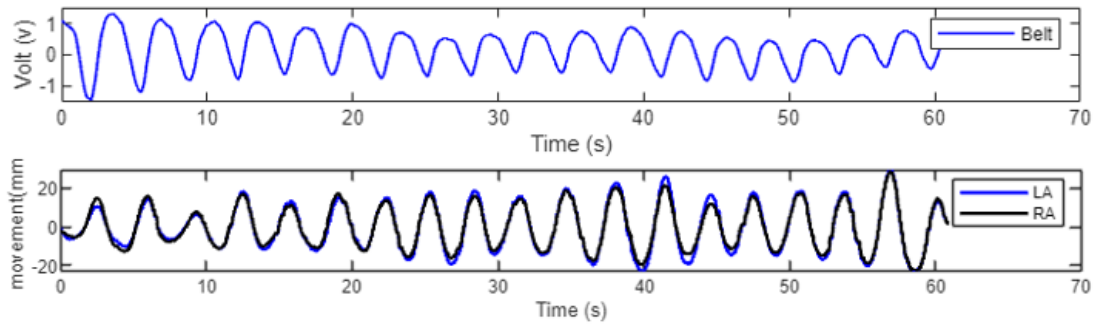

(b) Abdomen belt and RFID signal during breathing

Figure 5.1: Belt and bilateral tag signals of abdomen or chest respiration

Bilateral (Intra-region) Differences

In addition to regional differences, We also observed notable bilateral variations when two RFID tags were placed symmetrically within the same anatomical region, which were not expected. While waveform shapes were generally consistent, the amplitudes sometimes diverged considerably between the two sides. For instance in Figure 5.2, in one chest trial, the left upper thoracic tag recorded an average displacement of 13.78 mm, whereas the right upper thoracic tag recorded only 5.81 mm. Similarly, abdominal measurements occasionally showed left–right discrepancies, such as 21.68 mm versus 10.1 mm. These intra-region inconsistencies may result from small differences in tag placement, asymmetric tissue compliance, variations in electromagnetic coupling with the reader, or intrinsic differences between individual RFID tags.

Although the RFID system is capable of extracting respiratory rhythms, it sometimes exhibits deviations in representing the amplitude of chest and abdominal movements during inspiration and expiration. In some cases, the measured displacement can be approximately three times greater than the physiological norm. This discrepancy may be partly due to the radiative characteristics and structural limitations of the tag itself. The commercial RFID tags used in this experiments were originally designed for general-purpose environments and were not optimized for placement on human skin. The dielectric properties of the skin and surrounding soft tissue can affect the antenna's radiation performance, thereby impacting the

tag's ability to sense subtle positional changes.

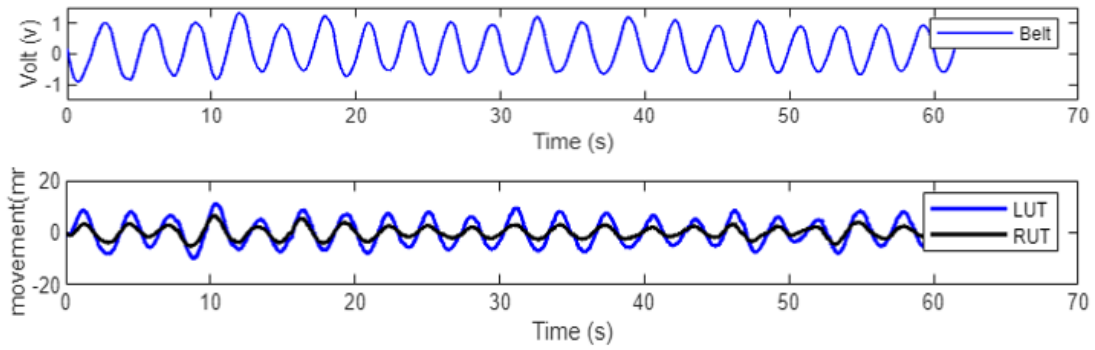

(a) Inconsistency between tags of chest

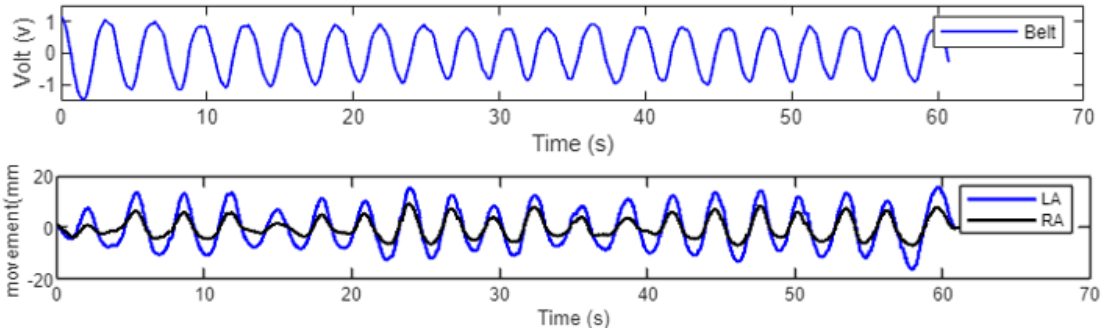

(b) Inconsistency between tags of abdomen

Figure 5.2: Disagreement in bilateral tag signals of abdomen or chest respiration

5.1.1 Considerations on Tag Deployment

In the initial experimental design, six RFID tags were planned to be deployed at distinct anatomical sites across the chest and abdomen—specifically, the right upper thorax (RUT), left upper thorax (LUT), right lower thorax (RLT), left lower thorax (LLT), right abdomen (RA), and left abdomen (LA) to comprehensively capture multidimensional respiratory motion. However, preliminary experiments consistently revealed unstable signal strength from at least two of the six tags. These tags frequently exhibited weak or intermittent readings, likely due to suboptimal contact with the skin, inconsistent electromagnetic coupling, or partial obstruction caused by body curvature or posture at certain locations. To improve data reliability and simplify the experimental configuration, we reduced the number of active tags, testing two simplified setups: a two-tag configuration and a four-tag configuration. These arrangements provided more stable and consistent signal acquisition without substantially compromising the fidelity of respiratory motion tracking. While this simplification was effective for the current study, it inherently limits spatial resolution and the ability to capture complex, multidimensional chest and abdominal movements.

5.1.2 Tag antenna fabrication

The fabrication and packaging processes of the RFID tags used in this experiment also have space for improvement. The current tags were manually attached, and traditional manufacturing methods may introduce issues such as poor positional repeatability, bending-induced deformation, and inconsistent conductive paths, all of which can compromise data stability and repeatability. To enhance system reliability and measurement precision, more refined manufacturing approaches could be adopted. These include inkjet printing with conductive ink to fabricate antennas or directly printing antenna patterns on flexible PCBs, both of which could improve tag consistency, adhesion, and electrical performance. Additionally, there exists substantial inter-individual variability in breathing patterns. Different breathing styles (e.g., thoracic vs. abdominal breathing) and pathological conditions (e.g., obstructive or restrictive pulmonary diseases) can alter respiratory behavior and waveform characteristics. Consequently, defining a universal threshold for abnormal pattern detection based on RFID signals remains challenging. Clinical assessment often requires a combination of physiological parameters and domain-specific knowledge. In this thesis, the abnormal detection threshold was conservatively defined based on exceeding the physiologically plausible range of displacement, serving primarily to eliminate motion-induced artifacts rather than for clinical diagnosis.

5.2 Future Work

The proposed RFID-based respiratory monitoring system has provided a clear framework and direction for non-contact assessment of breathing, however, several aspects require further improvement and resolution before practical deployment can be achieved. Current measurements occasionally overestimate chest and abdominal excursions by two to three times physiological limits, and bilateral recordings sometimes show inconsistent amplitudes between the left and right sides. These discrepancies may arise from subject-specific breathing habits, tag sensing limitations, dielectric influences of skin tissue, or placement variability, and future studies should clarify the reasons to improve measurement reliability. Moreover, the PZT belt used as the reference in this study is not ideally suited for validating geometric displacement, more accurate benchmarks should be proposed. The present signal analysis algorithm mainly rejects random motion artifacts beyond physiological ranges, but does not yet detect disease-related alterations in waveform period or amplitude; future developments should focus on extracting clinically relevant features to support diagnostic applications. On the hardware side, while antenna reflection coefficients indicated good impedance matching, the realized gain was relatively low (approximately -14 dBi), underscoring the need for improved antenna design to enhance efficiency and stability. In addition, manual fabrication introduced variability, suggesting that precise machine-based manufacturing methods such as inkjet printing or flexible PCB production should be adopted to ensure consistency. Finally, for clinical applications, optimized tags could be packaged into adhesive, bandage-like patches that enhance comfort, portability, and ease of placement, thereby facilitating reliable respiratory monitoring in both clinical and home healthcare environments.

6
Conclusion

Real-time monitoring of respiratory function has been addressed through the development of a passive UHF RFID-based system for non-invasive and localized measurement. Commercial RFID hardware combined signal processing enabled accurate extraction of respiratory features, with results showing close agreement with a reference PZT respiratory belt. Compact tag antennas were designed, optimized, and fabricated using different techniques, showing the possibility for on-body operation. Overall, the study provides a framework suggesting that RFID technology could serve as a low-cost and unobtrusive approach for respiratory monitoring, the methodology and findings can be extended to broader healthcare applications, including clinical respiratory monitoring and integration into IoT-based remote health platforms.

Bibliography

[1] Levine SM, Marciniuk DD. Global Impact of Respiratory Disease: What Can We Do, Together, to Make a Difference? Chest. 2022 May;161(5):1153-1154.

[2] Viegi, Giovanni et al. "Global Burden of Chronic Respiratory Diseases." Journal of aerosol medicine and pulmonary drug delivery vol. 33,4 (2020): 171-177.

[3] Al Wachami N, Guennouni M, et al. Estimating the global prevalence of chronic obstructive pulmonary disease (COPD): a systematic review and meta-analysis. BMC Public Health. 2024 Jan 25;24(1):297.

[4] Olsen, M. F. (2005). Chest physical therapy in surgery: A theoretical model about who to treat. *Breathe*, 1, 308–314.

[5] Quanjer, P. H., et al. (1993). Lung volumes and forced ventilatory flows. European Respiratory Journal, 6(Suppl 16), 5-40.

[6] Vitalograph. ERS and Polgar Normal Values. `https://vitalograph.com/resources/clinical-library/lung-function-reference-values/ers-and-polgar-normal-values`

[7] Moore, V. C. (2023). Pulmonary Function Tests. In: StatPearls. *NCBI Bookshelf*. `https://www.ncbi.nlm.nih.gov/books/NBK482339/`

[8] Fagevik Olsén, M., et al. Reliability of the Respiratory Movement Measuring Instrument. *Clin. Physiol. Funct. Imaging*, 2010.

[9] Hanning, C. D. (1978). Inductive plethysmography: a new respiratory monitoring technique. British Journal of Anaesthesia, 50(11), 1045-1047.

[10] Kotani, K., et al. (2002). Monitoring of respiratory movement by a wearable capacitive sensor. IEEE Transactions on Biomedical Engineering, 49(7), 718-720.

[11] Kondo, T., Arita, H., Ohta, Y., & Yamabayashi, H. (1989). Role of the mediastinum as a part of the chest wall: Analyzed by computed tomography. *Respiration*, 56, 116–126.

[12] Hanning, C. D., Smith, H. C., & Ledingham, I. M. (1978). Clinical application of inductive plethysmography. *Scottish Medical Journal*, 23, 310–311.

[13] Kotani, T., Hanaoka, M., Hirahara, S., Yamanaka, H., & Tashiro, M. (2002). Ultrasonographic evaluation of the diaphragm movement. *Journal of Clinical Ultrasound*, 30(3), 158–162.

[14] Leong, A. Y., Farrell, M. J., Helme, R. D., & Gibson, S. J. (1999). The relationship between medical comorbidity and self-rated pain, mood disturbance, and function in older people with chronic pain. *The Journals of Gerontology Series A: Biological Sciences and Medical Sciences*, 54(1), M4–M10.

[15] K. Finkenzeller, *RFID Handbook: Fundamentals and Applications in Contactless Smart Cards, Radio Frequency Identification and Near-Field Communication*, 3rd ed., Wiley, 2010.

[16] Leong, K. S., & Ng, M. L. (1999). A study of the phase variation of RFID signals for motion detection. In Proceedings of the 1999 IEEE International Symposium on Industrial Electronics (Vol. 2, pp. 1106-1110).

[17] Yang, Y., & Cao, J. (2020). Robust RFID-based respiration monitoring in dynamic environments. In *2020 17th Annual IEEE International Conference on Sensing, Communication, and Networking (SECON)* (pp. 1–9). IEEE.

[18] Zang, C., Zhang, C., Zhang, M., & Niu, Q. (2022). An RFID-Based Method for Multi-Person Respiratory Monitoring. *Sensors*, 22(16), 6166.

[19] Gabriel, S., Lau, R. W., & Gabriel, C. The dielectric properties of biological tissues: III. Parametric models for the dielectric spectrum. *Phys. Med. Biol.*, 1996.

[20] S. Zhang, X. Liu, Y. Liu, B. Ding, S. Guo and J. Wang, "Accurate Respiration Monitoring for Mobile Users With Commercial RFID Devices," in IEEE Journal on Selected Areas in Communications, vol. 39, no. 2, pp. 513-525, Feb. 2021, doi: 10.1109/JSAC.2020.3020604. keywords: Monitoring;Radiofrequency identification;Wireless fidelity;Acoustics;Biomedical monitoring;Wireless sensor networks;In-home heathcare;breath monitoring;RFID;Internet of Things,

[21] Avery Dennison Company RFID Technology `https://rfid.averydennison.com/zh/home/explore-rfid/rfid-technology-basics.html`

[22] R. Want, An introduction to RFID technology, *IEEE Pervasive Computing*, vol. 5, no. 1, pp. 25–33, 2006.

[23] Impinj company, types of RFID Systems `https://www.impinj.com/products/technology/how-can-rfid-systems-be-categorized`

[24] EPCglobal Inc., EPC Radio-Frequency Identity Protocols Class-1 Generation-2 UHF RFID Protocol for Communications at 860 MHz–960 MHz Version 1.2.0, 2008.

[25] Zhang, J., Tian, G. Y., Marindra, A. M. J., Sunny, A. I., & Zhao, A. B. (2020). A review of passive RFID tag antenna-based sensors and systems for structural health monitoring applications. *Sensors*, 20(18), 5265.

[26] Marrocco, G. (2007). RFID antennas for the UHF remote monitoring of human subjects. *IEEE Transactions on Antennas and Propagation*, 55(6), 1862–1870.

[27] Bouhassoune, I., Saadane, R., & Minaoui, K. (2019). RFID double-loop tags with novel meandering lines design for health monitoring application. *Journal of Healthcare Engineering*, 2019, Article ID 5076139.

[28] Balanis, C. A. (2016). *Antenna Theory: Analysis and Design* (4th ed.). Wiley.

[29] Loo, C.-H., Elmahgoub, K., Yang, F., Elsherbeni, A. Z., Kajfez, D., Kishk, A. A., Elsherbeni, T., Ukkonen, L., Sydänheimo, L., Kivikoski, M., Merilampi, S., & Ruuskanen, P. (2008). Impedance matching for RFID tag antennas.

[30] Rao, K. V. S., Nikitin, P. V., & Lam, S. F. (2005). Antenna design for UHF RFID tags: A review and a practical application. *IEEE Transactions on Antennas and Propagation*, 53(12), 3870–3876.

[31] Zhang, S., Zhang, D., Xie, L., Wang, W., Wang, Y., & Li, Z. (2018). AutoTag: Recurrent Variational Autoencoder for Unsupervised Respiratory Monitoring

with RFID Tags. In *Proceedings of the IEEE Global Communications Conference (GLOBECOM)* (pp. 1–6). IEEE.

[32] Proakis, J. G., & Manolakis, D. G. (2006). *Digital Signal Processing: Principles, Algorithms, and Applications* (4th ed.). Pearson Prentice Hall.

[33] Mallat, S. (2008). *A Wavelet Tour of Signal Processing: The Sparse Way* (3rd ed.). Academic Press.

[34] PZT company `https://support.pluxbiosignals.com/wp-content/uploads/2021/11/Respiration_PZT_User_Manual.pdf`

[35] Chest wall motion during tidal breathing A. De Groote, M. Wantier, G. Cheron, M. Estenne, and M. Paiva Journal of Applied Physiology 1997 83:5, 1531-1537

[36] Avery Dennison Smartrac Bling UHF RFID tag, `https://rfid.averydennison.com/en/home/product-finder/bling.html`

[37] Fujimoto K, Morishita H. Design and practice of small antennas I. In: Modern Small Antennas. Cambridge University Press; 2014:92-265.

[38] Impinj Monza R6-P Tag Chip Datasheet V7, `https://support.impinj.com/hc/article_attachments/1500019253682/Impinj_Monza_R6-P_Tag_Chip_Datasheet_V7_20210514.pdf`

[39] Choi, Jeong, An, Chae. (2022). Development of an Online Monitoring Device for the Mixing Ratio of Two-Part Epoxy Adhesives Using an Electrical Impedance Spectroscopy Technique and Machine Learning. Processes. 10. 951. 10.3390/pr10050951.

[40] P. K. Sharma, N. Gupta and P. I. Dankov, "Analysis of Dielectric Properties of Polydimethylsiloxane (PDMS) as a Flexible Substrate for Sensors and Antenna Applications," in IEEE Sensors Journal, vol. 21, no. 17, pp. 19492-19504, 1 Sept.1, 2021, doi: 10.1109/JSEN.2021.3089827.

[41] M. Li and C. Yang, 'Conductive Adhesives as the Ultralow Cost RFID Tag Antenna Material', Current Trends and Challenges in RFID. InTech, July 20, 2011. doi: 10.5772/16623.

A

Appendix 1

A.1 Environmental Parameters in CST

Table A.1: Simulation setup and material parameters

Component	**Description**
Substrate Material	PDMS ($\varepsilon_r = 2.8$, $\tan\delta = 0.02$), thickness: 0.5 mm
Metal Layer	Copper, conductivity 5.8×10^7 S/m
Human Tissue Model	**Skin:** 1 mm, $\varepsilon_r = 43.8$, $\sigma = 0.6$ S/m **Fat:** 10 mm, $\varepsilon_r = 5.64$, $\sigma = 0.1$ S/m **Muscle:** 10 mm, $\varepsilon_r = 54.5$, $\sigma = 0.6$ S/m
Boundary Conditions	Open boundary
Port	Discrete port with a default impedance of 50 Ω
Mesh Setup	Hexahedral mesh; simulation iterated until S-parameter variation was less than 10^{-4} (–40 dB)

DEPARTMENT OF ELECTRICAL ENGINEERING
CHALMERS UNIVERSITY OF TECHNOLOGY
Gothenburg, Sweden
www.chalmers.se

CHALMERS
UNIVERSITY OF TECHNOLOGY